NEUROSCIENCE

Pathway-specific inputs to the superior colliculus support flexible responses to visual threat

Chen Li[1,2]†‡, Norma K. Kühn[1,2]‡, Ilayda Alkislar[1,3]§, Arnau Sans-Dublanc[1,2], Firdaouss Zemmouri[1,4], Soraya Paesmans[1,2], Alex Calzoni[1,2], Frédérique Ooms[1,5], Katja Reinhard[1,2]||¶, Karl Farrow[1,2,5]*¶

Behavioral flexibility requires directing feedforward sensory information to appropriate targets. In the superior colliculus, divergent outputs orchestrate different responses to visual threats, but the circuit organization enabling the flexible routing of sensory information remains unknown. To determine this structure, we focused on inhibitory projection (Gad2) neurons. Trans-synaptic tracing and neuronal recordings revealed that Gad2 neurons projecting to the lateral geniculate nucleus (LGN) and the parabigeminal nucleus (PBG) form two separate populations, each receiving a different set of non-retinal inputs. Inhibiting the LGN- or PBG-projecting Gad2 neurons resulted in opposing effects on behavior; increasing freezing or escape probability to visual looming, respectively. Optogenetic activation of selected inputs to the LGN- and PBG-projecting Gad2 cells predictably regulated responses to visual threat. These data suggest that projection-specific sampling of brain-wide inputs provides a circuit design principle that enables visual inputs to be selectively routed to produce context-specific behavior.

INTRODUCTION

Animals are born with a catalog of robust behaviors that facilitate quick and reliable responses to ecologically salient stimuli (*1*). While instinctive behaviors are often stereotyped, they can be surprisingly flexible; adapting to an animal's internal state, prior experience, and environmental conditions (*1*, *2*). This ability to change behavior depends on neural circuits that can alter their outputs in response to the same input. However, many innate behaviors rely on dedicated feedforward subcortical circuits involving the same sets of brain structures in different species (*2–6*).¶

In the early visual system, the superior colliculus has been demonstrated to be crucial for the processing of visual information that release innate behaviors (e.g., freezing, escape, and hunting) (*7–12*). For example, rapidly expanding spots reliably trigger defensive responses in a wide variety of animals including flies, fish, rodents, and primates (*13–18*). In rodents, the key neuronal circuits of the superior colliculus mediating visually evoked freezing and escape responses appear to be formed by dedicated pathways (*8*, *11*, *12*, *19*, *20*). These feedforward pathways show characteristics of being hard-wired, where distinct cell types receive different sets of inputs from the retina (*21*, *22*), and project to different sets of collicular targets (*11*, *12*, *23–25*). Together, this circuit architecture results in the relay of salient visual features and the triggering of behavior (*8*, *10–12*, *20*, *21*, *26*, *27*).

What features of the circuitry of the superior colliculus might support flexible behavioral responses to the same visual stimulus? The superior colliculus receives, in addition to inputs from the retina, input from a large proportion of the nervous system (*28–33*). These include inputs from the cortex (CTX), basal ganglia, thalamus (TH), and midbrain (MB) that provide information about context, internal state, or prior experience necessary to appropriately adjust an animal's response to the next exposure to the same stimulus (*34–36*). For example, inputs to the superior colliculus from the ventral lateral geniculate nucleus of the TH have been shown to encode anxiety levels that can be influenced by previous exposure to threat and modify the probability of responding to the next stimulus (*37*, *38*). In addition, inputs from the CTX to the superior colliculus alter the gain of visual responses and arrest behaviors (*7*, *39–41*). These findings suggest that non-retinal inputs could form a circuit basis for the flexible processing of visual information.

Here, we investigated two distinct populations of inhibitory *Gad2*-positive projection neurons (Gad2) in the mouse superior colliculus that project to the lateral geniculate nucleus (Gad2-LGN) and the parabigeminal nucleus (Gad2-PBG), respectively. The two populations encoded similar aspects of visual inputs and received similar sets of visual information from the retina. In contrast, Gad2-LGN and Gad2-PBG displayed different visual response strengths and sampled different sets of brain-wide inputs, where some inputs were shared, and others showed strong preferences for one pathway over the other. Inhibiting either of the two pathways directly or activating circuit-specific inputs to the colliculus had divergent effects on visually triggered behaviors. These data suggest that circuit-specific non-retinal inputs can modulate the driving, feedforward information about visual threat and modify behavioral reactions to repeated exposure of the same stimuli. Thus, cell type–specific sampling of inputs to the colliculus with segregated outputs provides the underlying circuit architecture to support flexible behavioral responses.

[1]Neuro-Electronics Research Flanders, VIB, Leuven, Belgium. [2]Department of Biology, KU Leuven, Leuven, Belgium. [3]Northeastern University, Boston, MA, USA. [4]Faculty of Pharmaceutical, Biomedical, and Veterinary Sciences, University of Antwerp, Antwerp, Belgium. [5]Imec, Leuven, Belgium.
*Corresponding author. Email: karl.farrow@nerf.be
†Present address: Department of Neuroscience, Yale School of Medicine, New Haven, CT, USA.
‡These authors contributed equally to this work.
§Present address: Neuroscience Graduate Program, University of California San Francisco, San Francisco, CA, USA.
||Present address: Scuola Internazionale Superiore di Studi Avanzati, Trieste, Italy.
¶These authors contributed equally to this work.

RESULTS

LGN- and PBG-projecting Gad2 cells are separate populations

The mouse superior colliculus is a layered structure where the superficial three layers [stratum zonale (SCzo), stratum griseum superficiale (SCsg), and stratum opticum (SCop)] contain retinorecipient neurons, which is subsequently referred to as the superficial superior colliculus (SCs) (3, 31). The SCs is composed of several molecularly defined cell types that each project to a distinct set of downstream targets (23, 24). One class of projection neurons, the Gad2⁺ neurons (Gad2), are GABAergic (23) and inhibit their target neurons (42). Gad2 neurons have been reported to send axons to the parabigeminal nucleus (PBG) in the MB and the lateral geniculate nucleus (LGN) of the TH (23, 43). To confirm this, we injected a Cre-dependent AAV (*AAV-flox-tdTomato-SypEGFP*) into the SCs of *Gad2-Cre* mice (44), expressing tdTomato in the cytosol and green fluorescent protein (GFP) at the axonal endings of Gad2 neurons (Fig. 1). Our injections predominantly labeled neurons in the SCs (82.4%), with some labeling in the adjacent intermediate layers (Fig. 1, A and B). As previously reported (23, 43), the strongest labeling of Gad2 projections is found in the ventral LGN (LGv) and PBG (Fig. 1, C to E). In addition, some local labeling is observed in the dorsal LGN (LGd) and diffuse labeling in the lateral posterior nucleus of the TH (LP) (Fig. 1, C and E). In the following experiments, retrograde labeling of Gad2 projection neurons was targeted to the LGN (LGd and LGv) and the PBG, but some labeling of the diffuse projections to the LP cannot be excluded (see Discussion).

To determine whether individual Gad2 cells project to both the PBG and the LGN, we performed retrograde labeling from the LGN and PBG by injecting Cre-dependent herpes simplex virus (HSV) coding for GCaMP6s (*HSV-flox-GCaMP6s*) or mCherry (*HSV-flox-mCherry*) in *Gad2-Cre* mice (Fig. 2A; see Methods). Our LGN injection was targeted to the dorsal LGd but led to infection of the ventral LGv as well (fig. S1, A and B). We found LGN- and PBG-projecting Gad2 cells (Gad2-LGN and Gad2-PBG) across many depths of the superior colliculus and have focused our analysis on the SCs. Gad2-LGN and Gad2-PBG were predominantly located in the hemisphere ipsilateral to the injection site (fig. S1C). In the SCs, the LGN-projecting and PBG-projecting Gad2 cells rarely overlapped (Fig. 2, B to D; double positive: 2.81 ± 0.80%; mean ± SEM, 26 sections from four animals). In the SCs, the LGN-projecting Gad2 cells were concentrated medially, while the PBG-projecting Gad2 cells were more evenly distributed along the medial-lateral axis (fig. S1D). Co-injection of *HSV-flox-GCaMP6s* and *HSV-flox-mCherry* into either the LGN or PBG resulted in extensive double labeling of neurons in the SCs, indicating that the two viruses can co-express fluorophores in the same neuron (fig. S1, E to H; double positive: 74.41 ± 2.65%; mean ± SEM, 16 sections from three animals). Together, these data indicate that SCs Gad2 cells consist of at least two distinct populations, one projecting to the LGN (Gad2-LGN) and the other to the PBG (Gad2-PBG).
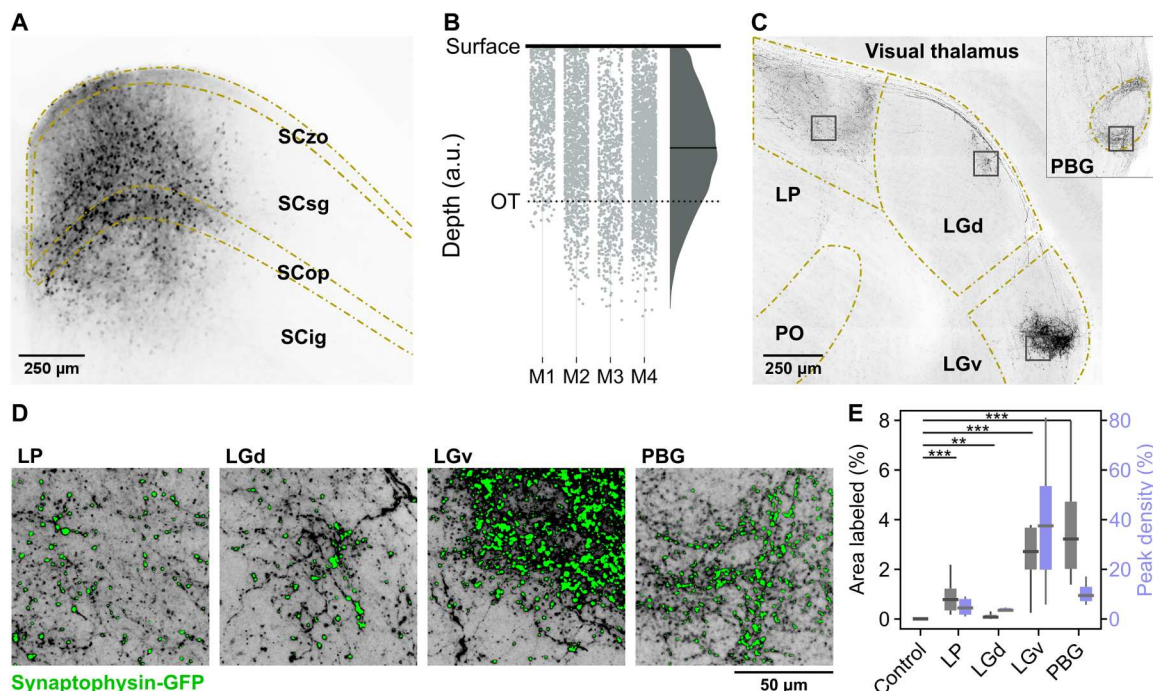

Fig. 1. Axonal targets of Gad2 projection neurons. (**A**) Example of labeling of Gad2 neurons in the SC after injection of *AAV-flox-tdTomato-SypEGFP*. (**B**) Quantification of the depth of labeled Gad2 neurons. Dot clouds are from individual animals. The violin plot is the distribution of all neurons. n = 5298 cells in 26 slices and four animals. OT, optic tract. a.u., arbitrary units. (**C**) Example image of axons in the thalamus and PBG. (**D**) Zoomed-in view of individual regions to show the presence of synaptic boutons in each region. (**E**) Quantification of normalized labeling density and peak density in each region. Thalamus, n = 11 slices and PBG, n = 8 slices in four animals. Control regions are neighboring thalamic nuclei, either PO, PoT, or VTM, depending on the position of the coronal slice. ***P < 0.001, **P < 0.01, Kruskal-Wallis test.
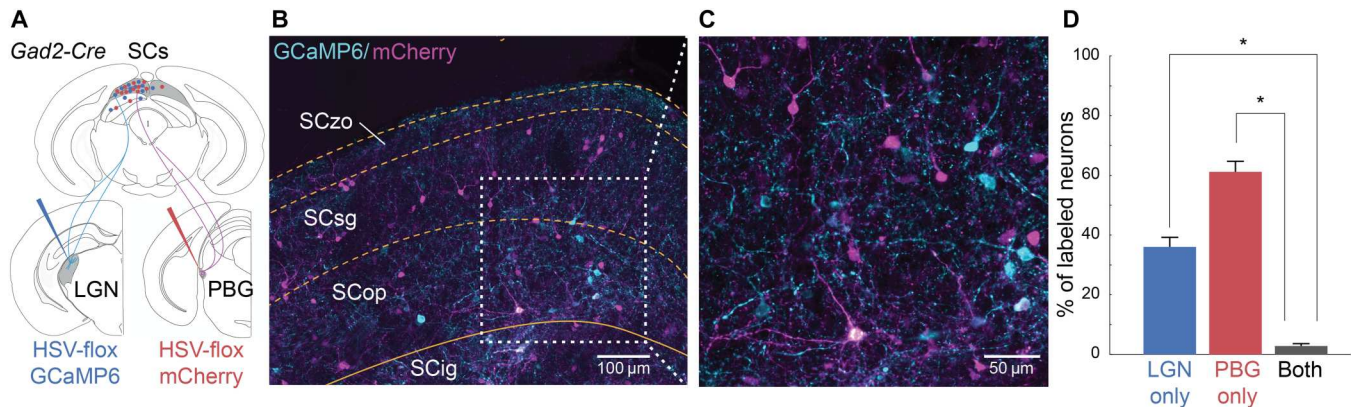
Fig. 2. Gad2 cells form two distinct projection-specific populations. (**A**) Schematic of retrograde virus injection strategy labeling different populations of Gad2 cells. (**B**) Example of labeled Gad2 cells in the superficial layers (SCzo, SCsg, and SCop) of the superior colliculus (SCs). LGN-projecting Gad2 cells: blue, GCaMP6+; PBG-projecting Gad2 cells: red, mCherry+. (**C**) Zoomed-in view of the white square from (B). (**D**) Quantification of the overlap between neurons labeled from the two locations (LGN only: 36.01 ± 3.22%; PBG only: 61.20 ± 3.53%; Both: 2.81 ± 0.80%. Twenty-six sections from $n = 4$ animals. All the data are shown as the means ± SEM (indicated by error bars). LGN only versus Both: *$P = 2.89 \times 10^{-9}$ PBG only versus Both: 2.87×10^{-9}, one-way ANOVA with post hoc multiple-comparison test. See also fig. S1.

LGN- and PBG-projecting Gad2 cells encode similar visual information

The strict separation of LGN- and PBG-projecting Gad2 cells suggests that the two populations might transfer different features of the world to their respective brain targets. To test this, we recorded visual responses of Gad2 neurons in head-fixed, behaving mice using two-photon calcium imaging (Fig. 3, A to E). To ensure projection-specific expression of the fluorescent calcium sensor GCaMP6s, we used a two-viral vector strategy combining *Cre-lox* and *FLP-FRT* conditional expression systems. First, an injection of a Cre-dependent retrograde virus into the projection area (PBG: *HSV-flox-FLP-mCherry*, LGN: a mix 3:2 of *HSV-flox-FLP* and *AAV-mCherry*) allowed for flippase (FLP) expression in Gad2 cells (Fig. 3A; see Methods). Subsequently, an FLP-dependent AAV (*AAV-flip-GCaMP6s*) injected into the superior colliculus led to expression of GCaMP6s in either Gad2-PBG or Gad2-LGN neurons. All in vivo two-photon imaging in the superior colliculus was performed at depths between 0 and 300 μm. A set of visual stimuli including expanding, shrinking, dimming, and sweeping spots of different speeds and sizes was presented to head-fixed mice that were free to run on a floating ball (Fig. 3B; see also Methods). We found that individual neurons responded to most of the visual stimuli presented (Fig. 3, C to E). When comparing the normalized peak responses to each stimulus, the two populations showed preferences for similar sets of visual stimuli, where each population showed the strongest responses to slowly sweeping spots and a bright looming disk (Fig. 3E and fig. S2).

We next applied Cre-dependent retrograde transsynaptic viral tracing to target the retinal ganglion cells that innervate Gad2-LGN and Gad2-PBG neurons, respectively (Fig. 3F and fig. S3, A and B). Injections of HSV expressing G-protein and TVA in a Cre-dependent manner (*HSV-flox-TVA-G-mCherry*) to either the LGN or PBG of *Gad2-Cre* mice were followed by injections of G-deleted rabies virus coated with envelope-A in the superior colliculus (*EnvA-RVΔG-GCaMP6f*), expressing a fluorescent calcium indicator in innervating retinal ganglion cells (see Methods). This allowed anatomical tracing (Fig. 3, G and H), molecular labeling

(Fig. 3I), and two-photon calcium imaging of the labeled retinal ganglion cells (Fig. 3J).

Our results show that, in accordance with the visual response properties of the two Gad2 populations, each circuit receives input from a similar set of retinal ganglion cell types. First, the labeled retinal ganglion cells from each circuit showed comparable morphologies; they cover a similar range of dendritic areas independent of the stratification depth (bistratified, stratifying outside the ChAT bands, and monostratified with dendrites below or above the ChAT bands) (Fig. 3, G and H, and fig. S3C). Second, histological staining showed that both LGN- and PBG-projecting Gad2 cells received input from a similar percentage of ON-OFF direction-selective cells (CART; LGN: 16.3% versus PBG: 15.1%, $n = 3$ retinas for each circuit), alpha cells (SMI32; LGN: 40.0% versus PBG: 38.6%, $n = 4$ retinas for LGN and $n = 3$ retinas for PBG), and F-cells (FOXP2; LGN: 5.90% versus PBG: 4.6%, $n = 1$ retina for LGN and $n = 3$ retinas for PBG) (Fig. 3I and fig. S3, D to H).

In addition, the population of retinal ganglion cells innervating the Gad2-LGN and Gad2-PBG circuits responded to similar sets of visual stimuli. Visual responses of labeled retinal ganglion cells were measured using two-photon calcium imaging and targeted patch-clamp recordings in explanted whole-mount retinas (see Methods and fig. S3, I to M). A set of visual stimuli including moving bars, expanding disks, and full-field flashes were presented and the responses of 393 retinal ganglion cells innervating the Gad2-LGN circuit ($n = 7$ mice) and 189 cells innervating the Gad2-PBG circuit ($n = 11$ mice) were recorded. Consistent with the CART staining result, we found that both circuits sampled from direction-selective cells (Fig. 3J). Similar examples of overlapping response types were found for all visual stimuli examined, including orientation-selective responses and various contrast responses such as ON-OFF, transient ON or OFF, and sustained ON or OFF responses (Fig. 3J and fig. S3M). Finally, both circuits received inputs from retinal ganglion cells with comparable response patterns to behaviorally relevant stimuli including looming and expanding disks (Fig. 3J), as well as a dimming disk (fig. S3M). Together, the retinal inputs to the Gad2-LGN and Gad2-PBG
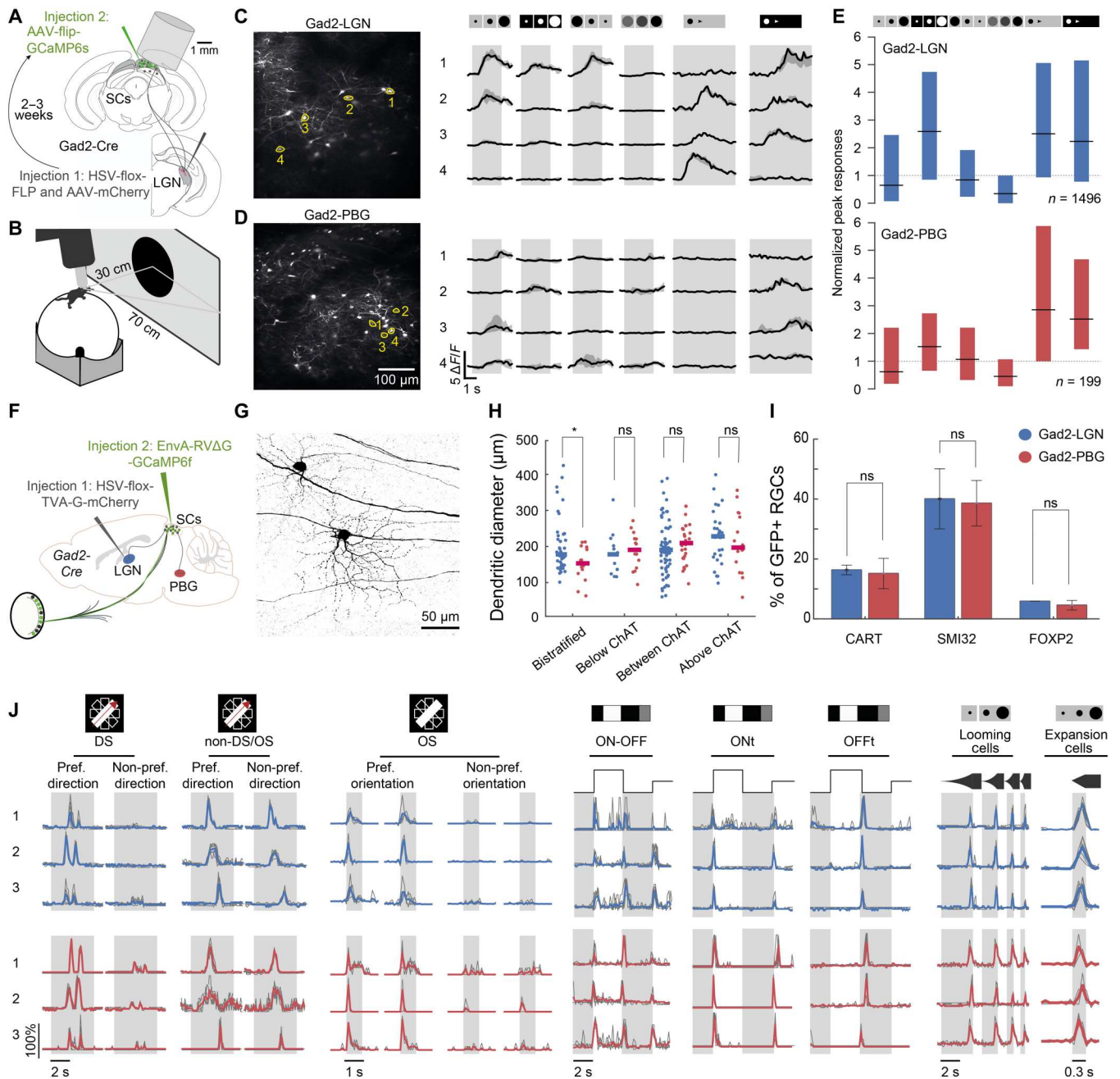
Fig. 3. LGN- and PBG-projecting Gad2 cells encode similar visual information. (**A**) Schematic of labeling strategy for in vivo 2p calcium imaging of Gad2-LGN and Gad2-PBG cells in the superficial superior colliculus (SCs). (**B**) Schematic of the in vivo recording setup. (**C** and **D**) Example recordings of Gad2-LGN (C) and Gad2-PBG (D) neurons. Left: Recording areas with highlighted example neurons. Right: Calcium responses of highlighted neurons to a set of visual stimuli that from left to right are dark expansion, bright expansion, dark shrinking, dimming, and sweeping (dark and bright). Lines and shaded areas show medians and interquartile range from 10 repetitions. Gray rectangles indicate stimulus duration. (**E**) Boxplots of normalized peak responses to visual stimuli that are normalized by the median peak response to all stimuli (indicated by the dashed line). Horizontal black lines and boxes indicate median and interquartile range, respectively. Data from four mice per cell population. More response properties in fig. S2. (**F**) Injection strategy to express GCaMP6f in circuit-specific retinal ganglion cell populations. (**G**) Example histological picture of labeled cells. (**H**) Dendritic diameter of retinal ganglion cells with different stratification patterns. Horizontal lines indicate medians. *$P < 0.05$ Wilcoxon rank sum test and two-sample Kolmogorov-Smirnov test. (**I**) Percentage of GFP+ cells with labeling of CART, SMI32, or FOXP2. Means ± SEM are shown. Two-proportion z test. (**J**) Example responses of retinal ganglion cells innervating the Gad2-LGN (blue) or Gad2-PBG (red) circuit. DS, direction-selective; OS, orientation-selective; ON, positive contrast; OFF, negative contrast; t, transient; s, sustained. See also fig. S3.

circuit are similar, resulting in comparable visual encoding properties in each Gad2 population.

LGN- and PBG-projecting Gad2 cells receive distinct sets of brain-wide inputs

In addition to the retinal inputs, the superior colliculus receives extensive inputs from other brain regions (*28*). To map the non-retinal inputs, the same transsynaptic labeling strategy as for the retina was used (Fig. 4A). We conducted systematic analyses by assigning raw microscopic images of labeled brain sections from each individual mouse brain to their corresponding atlas template of the Allen Brain Atlas with the MATLAB user interface SHARP-Track toolkit (*45*) (Fig. 4B and fig. S5A; details in Methods). In a subset of the experiments, we quantified the position of the starter neurons, i.e., those that could be identified to be co-expressing mCherry and GCaMP6. Starter neurons were found predominantly (83%) in the SCs (fig. S4).

We found that each circuit receives extensive brain-wide inputs (Fig. 4C and fig. S5B). After counting the labeled neurons, we calculated the proportion of neurons in seven major regions of the nervous system, including CTX, subcortex (sCTX), TH, hypothalamus (HYP), MB, hindbrain (HB), and cerebellum (CB). For each circuit, the major input regions are the CTX and the MB (Fig. 4D). In general, we found that there was a preference for innervation from the hemisphere ipsilateral to the injection site (Fig. 4, C and D). Specifically, the Gad2-PBG circuit sampled more from the ipsilateral CTX (ipsi versus contra, $P = 0.031$, one-sided t test), and the Gad2-LGN circuit received biased inputs from the ipsilateral sCTX ($P = 0.041$) and the ipsilateral HYP ($P = 0.039$). When comparing the two circuits, we found a trend toward stronger inputs from the sCTX to Gad2-LGN neurons (LGN versus PBG: $P = 0.074$) and a similar trend for MB inputs to Gad2-PBG neurons ($P = 0.089$). Furthermore, the Gad2-LGN circuit received more inputs from the contralateral CTX ($P = 0.016$) and TH ($P = 0.088$). Considering different rabies virus transfection efficiency, we also compared the result of two different rabies strains, CVS and SAD-B19, and found stronger labeling of the CTX with the CVS strain. However, the relative distribution of any input area between the two circuits (Gad2-PGB and Gad2-LGN) was similar independent of which virus strain was used (fig. S5C).

To compare the input strength of each circuit, we calculated the normalized density of circuit-specific inputs from individual areas. First, along the antero-posterior, dorsal-ventral, and medial-lateral axis, the input strength was similar between brains, suggesting consistent labeling of input areas (fig. S5D). To compare the relative input strength to Gad2-LGN versus Gad2-PBG, we computed a bias index, the logarithm of the ratio of inputs to Gad2-LGN and to Gad2-PBG (Fig. 4, E and F, and data S1). Of the 69 labeled areas, 51 showed a significant bias for either the Gad2-LGN or Gad2-PBG circuit (see Methods). For instance, a number of inputs from thalamic, hypothalamic, and subcortical areas preferentially innervate Gad2-LGN–projecting neurons (Fig. 4, H to J). This includes areas that have been previously associated with modulation of innate behaviors such as the posterior paralaminar nuclei of the thalamus [PPnT; (*10*)] and the paraventricular hypothalamus [PVH; (*46*)]. Exceptions, with stronger inputs from TH, HYP, and sCTX to the Gad2-PBG circuit, include the zona incerta [ZI; (*47*)], the LGv (*37*, *38*), and the ventromedial hypothalamus (VMH). Inputs from the CTX and MB contain a similar proportion of

areas with innervation biases for either the Gad2-LGN or Gad2-PBG circuit (Fig. 4G and fig. S5, E and F).

A number of brain regions including the PVH, the LGv, the PR, some cortical areas [anterior cingulate area (ACA) and infralimbic area (ILA)], and several MB nuclei send many axons (high normalized density) to Gad2 neurons in the SCs (Fig. 4, G to J). However, these areas do not necessarily constitute the main inputs to the two circuits (normalized percentage). For instance, while a large proportion of ILA neurons target LGN-projecting Gad2 cells, they form only 0.9% of all inputs to this circuit. Instead, the highest percentage of input neurons are located in the PAG [10.36% (PBG) and 7.67% (LGN)], cortical areas responsible for vision, cognition, and motor output (RSPdl: 4.39% and 4.35%, MOs: 4.21% and 4.00%, RSPv: 3.81 and 2.91%), the ZI (2.75% and 2.10%), and the midbrain reticular nucleus (MRN: 4.42% and 3.00%). LGN-projecting Gad2 neurons receive strong inputs from the hypothalamic nucleus PeVH (1.62%), the LSd (2.56%), and several cortical areas (VISp: 4.16%, ACAv: 3.65%, ACAd: 3.66%), while PBG-projecting Gad2 neurons are strongly innervated by the somatosensory cortex (SSp: 4.90%, SSs: 1.87%). Together, while we observed many common inputs, we found strong biases in the brain-wide inputs to the Gad2-PBG and Gad2-LGN neuronal populations in the superior colliculus.

Nuclei involved in innate behaviors or encoding of contextual information provide distinct inputs to Gad2-PBG and Gad2-LGN cell populations

Next, we investigated the distribution of inputs from brain areas that are involved in different aspects of innate behaviors or encode contextual information (Fig. 5). We found that both circuits receive comparable inputs from areas involved in encoding of brain state (Fig. 5, A and B; mean Gad2-LGN: 18%, Gad2-PBG: 14%, $P = 0.11$). Cognition-related areas preferentially innervated the Gad2-LGN circuit (nine biased toward Gad2-LGN versus one biased for Gad2-PBG), while the Gad2-PBG circuit received more motor-related inputs (mean Gad2-LGN: 24%, Gad2-PBG: 31%, $P = 0.029$). Inputs from sensory areas showed strong biases for each circuit (six biased for Gad2-LGN, eight biased for Gad2-PBG, Fig. 5, B to D). Gad2 projection neurons receive visual information from various cortical areas, the posterior pretectal nucleus (PPT), and the LGv. We found a trend toward stronger inputs from those areas to Gad2-LGN neurons (mean Gad2-LGN: 61% of all sensory areas, Gad2-PBG: 39%), particularly from posterior and lateral visual cortical areas (VISpl, VISl, and VISp). In contrast, the PBG-projecting Gad2 neurons received more inputs from somatosensory areas (mean Gad2-LGN: 23%, Gad2-PBG: 41%, $P = 0.018$) such as the somatosensory cortex (SSp and SSs). Only one area that encodes taste information (PB) provides inputs to both Gad2 cell populations and no olfactory brain areas project to Gad2 neurons.

Finally, we analyzed the innervation patterns of areas associated with innate behaviors (Fig. 5E). Most areas have a strong bias for one or the other Gad2 population. For instance, several motor-related areas that induce or modulate innate reactions to threat preferentially innervate Gad2-PBG neurons. This includes the substantia nigra pars reticularis (SNr), which facilitates orienting responses (*48*) and modulation of avoidance behaviors (*49*, *50*); the deep superior colliculus (SCd) and periaqueductal gray (PAG), which mediate escape and freezing behaviors (*8*, *51*); and deep nuclei of
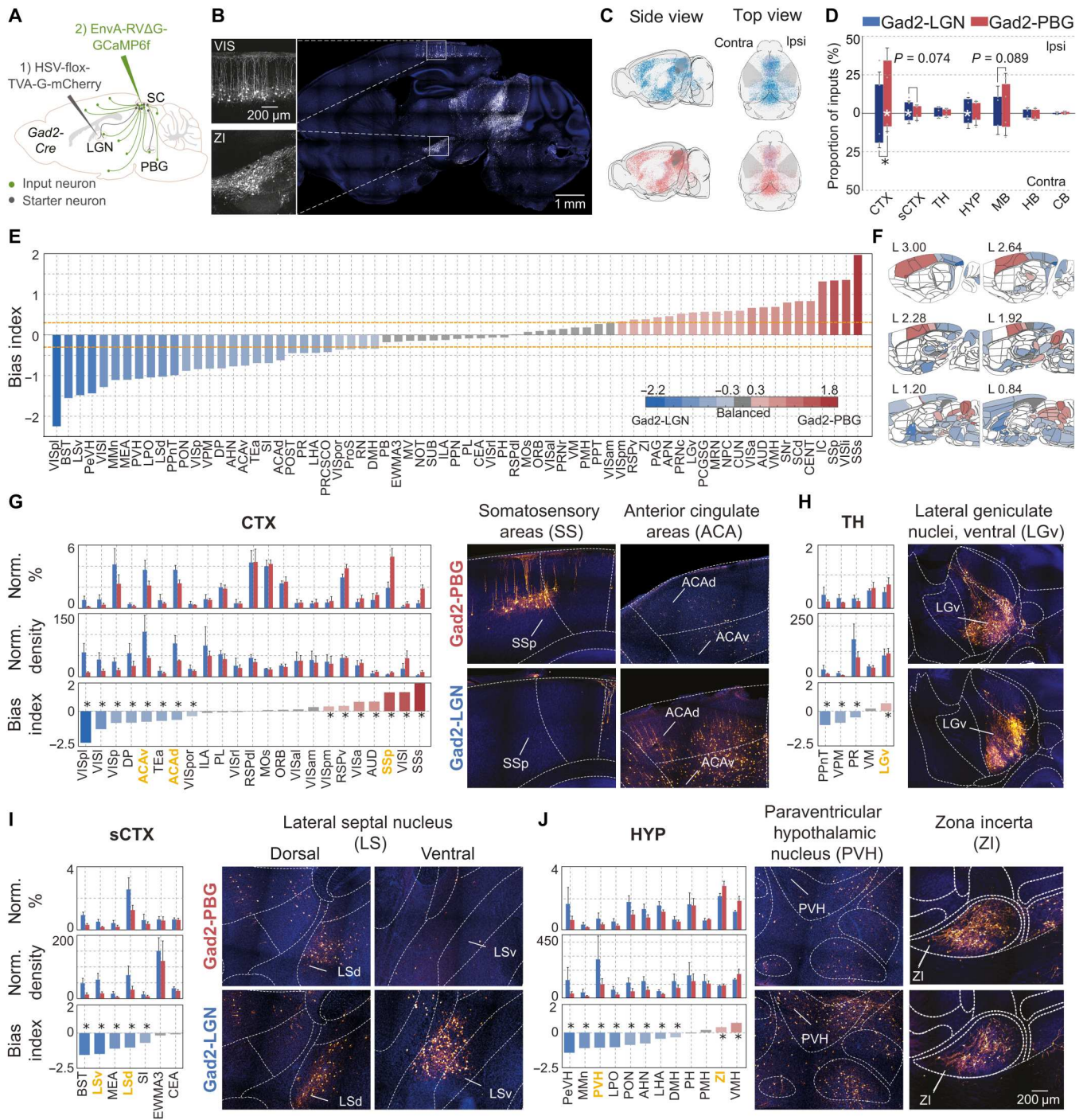
Fig. 4. Selective sampling of brain-wide inputs by LGN- and PBG-projecting Gad2 cells. (**A**) Schematic of the transsynaptic tracing method. (**B**) Example slices and brain areas showing the labeled neurons. (**C**) BrainGlobe 3D models of a subsample of labeled neurons from each circuit. (**D**) Percentage of input neurons of Gad2-PBG (red) and Gad2-LGN (blue) circuits across eight major brain regions. *$P < 0.05$ one-sided t test. Black stars are comparisons between circuits, and white starts are comparisons between hemispheres. (**E**) Summary of the bias index for each labeled brain area. The dashed line indicates the 95% confidence interval. Abbreviations can be found in data S1. (**F**) Example sagittal sections shown at different lateral positions (distance in millimeters from the midline). The color indicates the log ratio of the neuronal density. (**G** to **J**) Normalized percentage (top left), normalized density (middle left), and bias index (bottom left) for each area. (G) CTX, (H) TH, (I) sCTX, and (J) HYP for each circuit. Example histological sections are shown on the right of each panel. The scale bar of the ZI applies to all panels. See also figs. S4 and S5, table S1, and data S1 and S2.
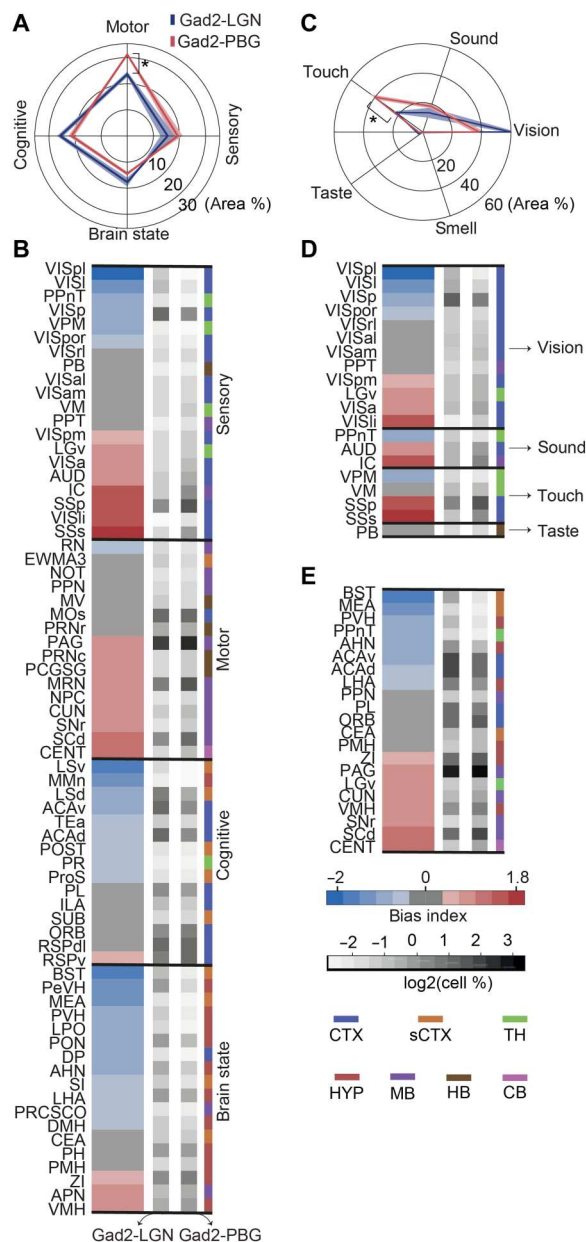
Fig. 5. Brain-wide inputs implicated in innate behavior modulation and contextual information selectively innervate LGN- and PBG-projecting Gad2 cells. (**A** and **B**) Inputs from major functional groups of brain areas. (A) Mean ± SEM of the normalized percentage of each input class for Gad2-PBG and Gad2-LGN. (B) Heatmap depicting the bias index of each area as shown in Fig. 4E, sorted separately for each functional class. Normalized densities for each circuit are indicated in gray. Major brain regions are depicted on the right. (**C** and **D**) Inputs from sensory areas. (**E**) Inputs associated with innate behaviors. *P < 0.05 one-sided t test. See also table S1 and data S1 and S2.

the cerebellum (central lobule, CENT). Biased inputs to Gad2-LGN neurons are associated with emotions, stress, and control of other autonomic functions [bed nuclei of the stria terminalis (BST), medial amygdala nucleus (MEA), and PVH] (52–54).

LGN- and PBG-projecting Gad2 cells are differently modulated by locomotion

Neurons in the visual system, including the superior colliculus, are often influenced by behavior (55–58). Therefore, we next determined whether the biased brain-wide inputs to LGN- and PBG-projecting Gad2 cells correspond with differential modulation by behavior in each group. We focused on the influence of locomotion in the form of running speed, measured alongside the neural responses during visual stimulation (Fig. 6A). We determined how strongly each neuron responded to running by measuring the mean response to the onset of running after the mouse had remained still for a minimum of 5 s (Fig. 6B). While both populations contain neurons that show clear responses to the onset of running, PBG-projecting neurons contain a much higher proportion of up-modulated neurons than the LGN-projecting population (Fig. 6B). When comparing the response to visual stimulation with the responses to motion onset, it is clear that LGN-projecting Gad2 cells show much stronger responses to visual stimuli, while PBG-projecting neurons show stronger responses (positive and negative) to the onset of locomotion (Fig. 6, C and D, P < 0.001, Kolmogorov-Smirnov test). This translates into a strong modulation of the visual responses of Gad2-PBG neurons by locomotion (fig. S6).

The strong modulation by locomotion of Gad2-PBG cells is corroborated by correlating neural responses with the running speed across the experiment. Both populations showed correlations that were significantly different from correlations with time-shuffled speed traces (Fig. 6E). However, PBG-projecting Gad2 cells showed a stronger bias for positive correlations with running [mean difference 0.115 with (0.0844, 0.145) 95% CI, P < 0.001, two-sided permutation t test]. The strong modulation of PBG-projecting Gad2 cells by locomotion corresponds well with the observed biases of motor inputs to this circuit.

Behavioral outputs of the LGN- and PBG-projecting Gad2 cells are different

Mice show strong innate behavioral responses to threatening stimuli (14, 17). To investigate whether the two target-specific populations of Gad2 cells play different roles in innate behaviors, we blocked these pathways using DREADDs (Designer Receptors Exclusively Activated by Designer Drugs) (59, 60). We selectively expressed a modified form of the human M4 muscarinic receptor (hM4Di) in either the LGN- or PBG-projecting Gad2 cells, using a double conditional strategy (Fig. 7, A and B, and fig. S7, A and B; see Methods). Neuronal activity of labeled neurons can be suppressed by its agonist clozapine N-oxide [CNO; (61)]. On the day of the behavioral test, 30 min after the systemic injection of CNO (2 mg/kg, intraperitoneal), mice were allowed to explore an arena for at least 5 min (Fig. 7C). Then, threat-like stimuli were presented: We used a looming stimulus consisting of 15 repetitions of an expanding dark disk that lasted 15 s in total and a sweeping stimulus, consisting of 1 repetition of a small dot moving from one side to the other side of the arena within 4 s (fig. S7C; see Methods). These two visual stimuli were shown multiple times in a random sequence on the monitor above the animal. The animal's motion was recorded using a camera below the arena (Fig. 7C) and extracted off-line with DeepLabCut (62) (see Methods and fig. S7D).

In response to the looming visual stimuli, mouse behavior was classified as either freezing (movie S1), escape (movie S2), or other (fig. S7, E and F). We calculated the proportion of observed
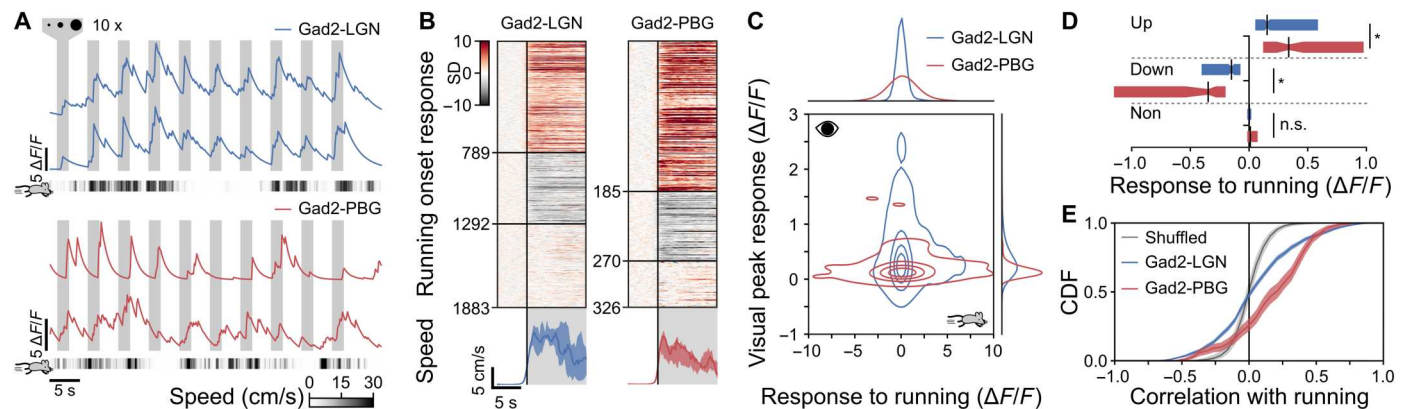
Fig. 6. LGN- and PBG-projecting Gad2 cells are differently modulated by locomotion. (**A**) Example responses to looming and locomotion of LGN-projecting (top) and PBG-projecting (bottom) Gad2 cells. Shaded areas indicate looming duration, and heatmaps below each block show running speed. (**B**) Top: Heatmaps of normalized (by SD), baseline-subtracted responses to onsets of running (preceded by >5 s of not running). Grouping by mean response during running into up-modulated (>1), down-modulated (<−1), and non-modulated (else). Bottom: Median running speed and interquartile range from all running onset events. (**C**) Gaussian kernel fit distribution of mean peak responses to visual stimuli and modulation by running events. Two-dimensional fit shows levels including 5, 25, 50, 75, and 95% of values. (**D**) Background-subtracted mean running response of groups in (B). Boxes, vertical lines, and indents show interquartile range, median, and confidence interval of the median, respectively. *$P < 0.001$ from two-sample Kolmogorov-Smirnov test. (**E**) Cumulative density functions of Pearson correlation coefficients between neural responses and running of the full experiment. Gray curve from shuffled speed traces. Shaded areas indicate confidence interval. Gad2-LGN and Gad2-PBG means are significantly different, $P < 0.001$, two-sided permutation t test. Data from $n = 4$ mice for each labeled population. See also fig. S6.

behaviors in response to the first trial of the looming stimulus and found that control mice ($n = 19$) injected with saline showed a strong preference for escape behaviors (Fig. 7, D and E). However, inhibiting the LGN-projecting Gad2 cells led to more freezing responses ($n = 15$; Gad2-LGN versus CTR: $P < 0.001$; Gad2-PBG versus CTR: $P < 0.001$), and inhibiting the PBG-projecting Gad2 cells increased the likelihood of escape responses to a looming stimulus ($n = 12$; Gad2-LGN versus CTR: $P < 0.001$; Gad2-PBG versus CTR: $P < 0.001$) (Fig. 7E and fig. S7, G and H). Reactions to a sweeping stimulus were affected with a similar bias: freezing responses increased during inhibition of Gad2-LGN–projecting cells, while some animals escaped during Gad2-PBG inhibition (fig. S7, I and J). Escape reactions were rarely observed in the control group (fig. S7K). The observed circuit-specific patterns were confirmed by a set of parameters: We found that the distance travelled during stimulus presentation (0–3 s) was shorter when inhibiting Gad2-LGN cells compared to controls and Gad2-PBG inhibition (median CTR: 47.3 cm, Gad2-LGN: 9.6 cm, Gad2-PBG: 68.9 cm; CTR versus Gad2-LGN: $P = 0.054$; Gad2-PBG versus Gad2-LGN: $P = 0.004$; Kruskal-Wallis test; Fig. 7F). During the stimulus, control and Gad2-PBG–inhibited animals ran predominantly toward the shelter (distance to shelter decrease CTR: $P = 0.006$; Gad2-PBG: $P = 0.002$, Wilcoxon rank sum test; Fig. 7G). When comparing animals of each group that showed freezing behavior, we found that Gad2-LGN–inhibited mice froze for a prolonged duration (median freezing time CTR: 3 s; Gad2-LGN: 7.5 s; CTR versus Gad2-LGN: $P = 0.04$, Kruskal-Wallis test; Fig. 7H). Similarly, we found a tendency toward longer escape latencies in the few escaping Gad2-LGN–inhibited animals (median latency CTR: 4.7 s, Gad2-LGN: 4.5 s, Gad2-PBG: 3.6 s; Fig. 7I). In conclusion, decreasing inhibition to the PBG increases escape behaviors, while decreasing inhibition to the LGN increases the probability and duration of freezing. These findings demonstrate that while inhibitory output circuits of the colliculus are not necessary to drive innate behaviors, the degree of activation of each pathway

changes the probability of which behavior, escape or freezing, is triggered by aversive visual stimuli.

Activation of input brain areas causes circuit-specific changes in behavior patterns

To test whether non-retinal inputs to the colliculus predictably modify the balance between freezing and flight, we activated circuit-specific input from two areas during the presentation of overhead visual stimuli in freely moving animals. The two areas chosen for manipulation were the ACA, which provides preferred input to Gad2-LGN–projecting cells, and the ZI, which has a bias for the Gad2-PBG circuit.

Transsynaptic rabies tracing was used to express Channelrhodopsin-2 (ChR2) by first injecting a floxed helper virus into the LGN or PBG [*HSV-floxed-TVA-G(CVS)-mCherry*] and, second, a *Channelrhodopsin-2* encoding rabies vector into the superior colliculus (*EnvA-RVΔG-ChR2-YFP*) (Fig. 8A, see Methods). We found that ACA and ZI inputs to the two circuits were distributed differently (fig. S8). Gad2-LGN cells received inputs from anterior-ventral ZI neurons (fig. S8A) and more lateral ACA neurons compared to the Gad2-PBG circuit (fig. S8B). During experiments, ChR2-expressing neurons in either the ACA or ZI were activated for periods of 20 s via optic fibers implanted bilaterally in the ACA or unilaterally above the ZI (Fig. 8B and fig. S9). Soon after the optogenetic stimulus began and when the animal entered the threat zone, the visual looming stimulation was started and lasted for 15 s. Optogenetic stimulation started at least 0.7 s before the visual stimulus and covered at least the first 6.5 s of the stimulation period. ChR2 expression and fiber placement were checked postmortem (Fig. 8C). We extracted the mouse position and calculated the running speed during the presentations of the looming stimulus (Fig. 8D) as described for previous behavior experiments (see Methods).

We found that optogenetically activating ACA or ZI inputs to the superior colliculus had circuit-specific effects on behavior. First,
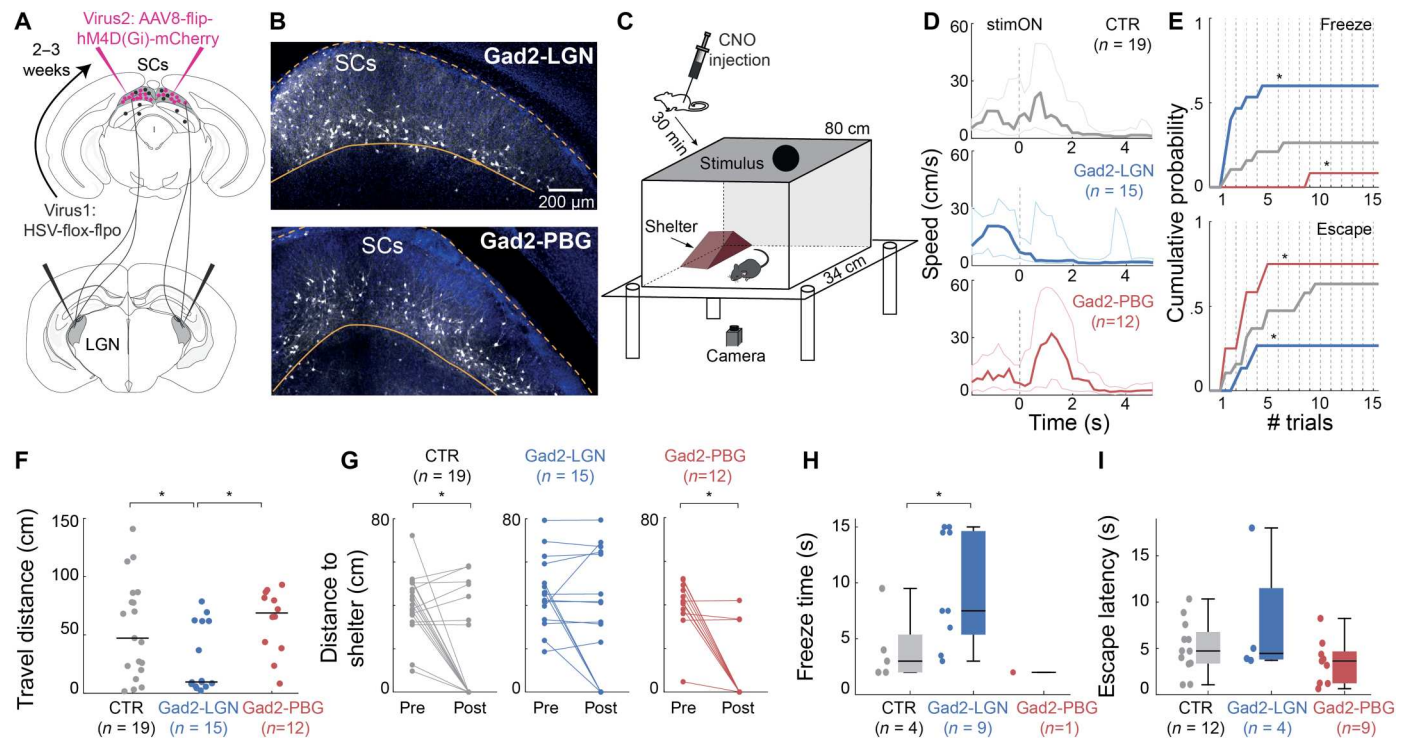
Fig. 7. LGN- and PBG-projecting Gad2 cells differently modulate looming-triggered defensive behaviors. (**A**) Schematic showing the virial strategy to specifically express hM4Di in either the LGN- or the PBG-projecting Gad2 cells. (**B**) Example brain slices showing the hM4Di expression (conjugated with mCherry, gray) in either the LGN-projecting (top) or the PBG-projecting cells (bottom). (**C**) The setup for behavioral test. (**D**) The median speed of all animals in each experimental group. Thin lines indicate 25% and 75% percentiles. Time 0 indicates the onset of the visual stimulus. (**E**) Cumulative probability of freezing (top) and escape (bottom) in the Gad2-LGN–inhibited (blue) and Gad2-PBG–inhibited (red) animals, and the control group (CTR, gray). *$P < 0.01$ two-sample Kolmogorov-Smirnov test. (**F**) Travel distance during 3 s after the looming stimulus. Horizontal lines indicate the median distance traveled. (**G**) Comparison of the distance before and during the looming stimulus. (**H**) Freezing time for freezing animals only. (**I**) Escape latency for escaping animals only. See also fig. S7 and movies S1 and S2.

activation of either the ACA or ZI inputs to the Gad2-LGN circuit decreased the probability of eliciting a reaction to visual threat (Fig. 8E) (CTR $n = 36$ of total trials, ACA-Gad2-LGN $n = 16$, ZI-Gad2-LGN $n = 15$ CTR versus ACA-Gad2-LGN $P < 0.001$; CTR versus ACA-Gad2-LGN $P = 0.005$). Second, when a behavior was triggered, the relative occurrence of freezing and flight tended to be different, compared to controls, for all manipulations [Fig. 8F; CTR $n = 18/12$ (escape/freezing); ACA-Gad2-PBG $n = 1/5$; ZI-Gad2-LGN $n = 1/4$; ZI-Gad2-PBG $n = 6/2$]. Projection neurons from the ACA to the colliculus are likely excitatory pyramidal neurons (Fig. 8C), while ZI inputs are predominantly GABAergic (*28*, *63*). Given that inhibition of the Gad2-PBG and the Gad2-LGN circuit facilitates escape and freezing, respectively (Fig. 7E), activation of these circuits would be expected to have the opposite effect on behavior. Activating excitatory ACA inputs to the Gad2-PBG circuit (i.e., increasing inhibitory drive to the PBG) increased the probability of freezing compared to activation of ACA inputs to the Gad2-LGN circuit (Fig. 8G) ($P < 0.001$ two-sample Kolmogorov-Smirnov test). On the other hand, stimulation of the inhibitory inputs from the ZI (i.e., decreasing inhibitory drive to the PBG or LGN) mimicked the effect of the chemogenetic inhibition of each circuit observed in Fig. 7. Activation of ZI inputs to the Gad2-PBG circuit led to a relative increase in escape behaviors, and activation of the ZI inputs to the Gad2-LGN led to a relative increase in freezing (Fig. 8H and fig. S9) (escape: $P < 0.001$; freeze: $P < 0.001$ two-

sample Kolmogorov-Smirnov test). Together, we found that activation of single non-retinal inputs predictably modifies the balance of visually evoked freezing and flight behaviors as expected based on the innervation bias of each input to the Gad2-LGN or Gad2-PBG circuits, and the results of our chemogenetic experiments (Figs. 4 and 7).

DISCUSSION

We describe the projection-specific logic by which the superior colliculus samples brain-wide inputs, providing a circuit design principle that enables the feedforward transfer of visual threat to be appropriately routed to trigger context-dependent behavior. Combining transsynaptic circuit tracing with two-photon imaging and pathway-specific manipulations, we compared the anatomical and functional input structure to two distinct populations of inhibitory projection neurons (Gad2-LGN or Gad2-PBG) in the superior colliculus. We showed that while the LGN- and PBG-projecting Gad2 cells encode similar aspects of the visual scene (Fig. 3), each population samples distinct sets of non-retinal inputs from other brain regions (Figs. 4 and 5), corresponding with the differential modulation of visually evoked activity in each circuit (Fig. 6). Independent chemogenetic inhibition of the Gad2-LGN and Gad2-PBG pathways shifted the behavioral response to overhead stimuli toward freezing and escape, respectively (Fig. 7). In addition,
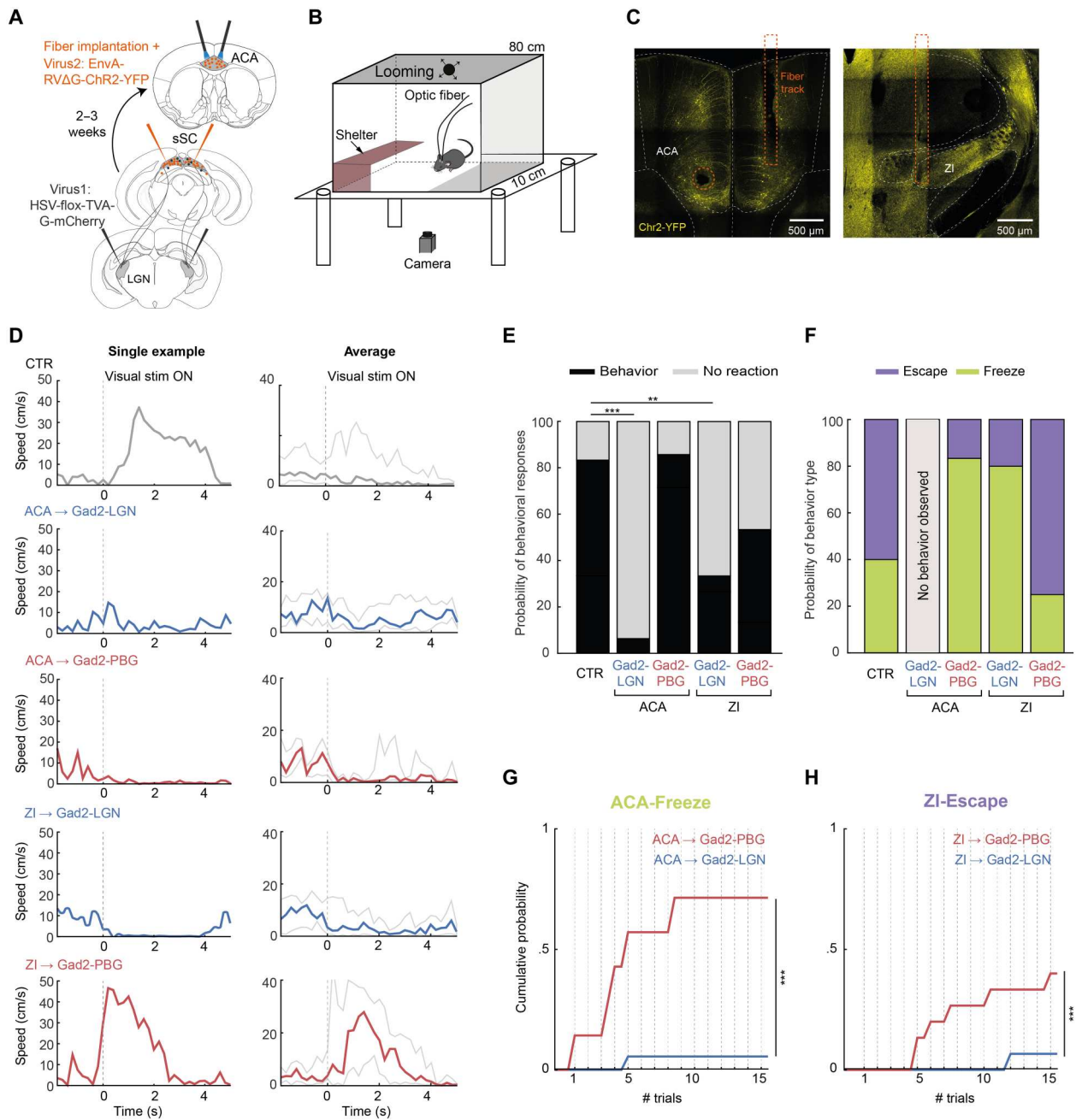
Fig. 8. Optogenetic activation of inputs to LGN- and PBG-projecting Gad2 cells predictably regulates responses to visual threat. (**A**) Schematic showing the viral strategy to specifically express ChR2 in the input brain regions to either the LGN- or the PBG-projecting Gad2 cells. (**B**) The setup for behavioral testing. (**C**) Histological section showing the expression of YFP conjugated with ChR2 in the anterior cingulate area (ACA) and zona incerta (ZI) and fiber positions. For the ACA, the two fibers were inserted at different angles (see fig. S7A). (**D**) Example (left) and average (right) speed traces in control animals and during different manipulations. (**E**) Percentage of looming stimulation trials leading to any type of innate behavior. One hundred percent corresponds to $n = 36$ trials from $n = 18$ animals (CTR), $n = 16/8$ (ACA-Gad2-LGN), $n = 7/4$ (ACA-Gad2-PBG), $n = 15/7$ (ZI-Gad2-LGN), and $n = 15/5$ (ZI-Gad2-PBG). **$P < 0.01$, ***$P < 0.001$ Fisher's exact test with Bonferroni correction. (**F**) Distribution of escape and freezing behavior. One hundred percent corresponds to all trials with behavior [black in (E)]. (**G**) Cumulative probability of freezing behavior during optogenetic activation of ACA inputs to each circuit. (**H**) Cumulative probability of escape behavior during optogenetic activation of ZI inputs to each circuit. ***$P < 0.001$ two-sample Kolmogorov-Smirnov test. See also figs. S8 and S9.

optogenetic activation of select inputs to each circuit affected the behavioral responses of the animals consistent with which pathway they innervated (Fig. 8). Our findings suggest that projection-specific sampling of brain-wide inputs provides a circuit design principle that supports the flexible response to the same visual stimuli by enabling selective gain control of different output pathways of the superior colliculus (Fig. 9).

Projection targets define two populations of Gad2 cells with distinct roles in behavior

The retino-recipient neurons of the mouse superior colliculus consist of morphologically, functionally, and genetically defined cell types that project to distinct sets of downstream targets (12, 23–25, 43, 64–66). Aside from wide-field neurons, which exclusively project to the LP, each class of neurons has been reported to project to at least two downstream targets (12, 23, 24). Here, using projection-specific retrograde labeling, we reveal that Gad2 projection neurons in the SCs are composed of at least two separate populations, one projecting to the LGN (predominantly the LGv) and the other to the PBG (Fig. 2). This is consistent with the different distributions of cell bodies found of retrogradely labeled Gad2 neurons in the superior colliculus projecting to either the Pbg or LGv by Whyland et al. (43). It is likely, given the diversity of dendritic anatomies and visual response properties observed in the populations of inhibitory projection neurons, that each projection is composed of more than one subtype (23, 43).

There are conflicting reports about where within the visual TH Gad2 neurons of the superior colliculus project (23, 43). Here, we observed that while most Gad2 neurons in the SCs innervate the LGv, there are diffuse projections to the LP and a focal projection to the LGd (Fig. 1). Previous reports have not described that the LP receives input from Gad2 neurons of the SC (23, 43). However, diffuse axonal labeling is visible in the histological image of figure 8a in Gale and Murphy (23). It remains to be determined whether the projections to different thalamic nuclei originate from different layers of the SC or whether collaterals of single neurons innervate the LGd, LGv, and LP. In addition, it has been suggested that the putative Gad2 projections to LGd are a consequence of transsynaptic labeling via the pretectum (43). In our experiments, while we

observe some axons in the LGd, we do not observe labeling of cell bodies in the pretectum using our double conditional labeling strategy (fig. S7).

In addition to projecting to distinct targets, different classes of neurons and different output pathways of the superior colliculus play distinct roles in visually guided orienting and defensive behaviors in mice (6, 8–12, 20, 39). Here, we demonstrate, using pathway-specific inhibition, that the role of Gad2 neurons projecting to the PBG and LGN are different. Whereby chemogenetic inhibition of Gad2-LGN neurons results in more and prolonged freezing responses to the presentation of looming stimuli, inhibition of Gad2-PBG neurons results in an increased probability of escape. These results are consistent with previous optogenetic activation experiments in two important ways. First, selective activation of excitatory projections to the PBG results in escape behaviors (12), which is in accordance with the increase in escape we observed when removing inhibition to the PBG. Second, while the role of the colliculo-LGN circuit in innate behavior has not been previously investigated, arrest and freezing behaviors can be induced by activating various sets of neurons in the colliculus (10, 12, 20). Given that we observe the diffuse Gad2 projections to the LP, we cannot exclude that freezing behavior is modulated by these projections. Together, we found that the two populations of projection-defined inhibitory neurons—Gad2 cells—were involved in modulating behavior in response to the presentation of an overhead visual stimulus.

Gad2 cell populations receive distinct sets of brain-wide inputs, but share visual properties

Output circuits of the colliculus that drive different innate behaviors have been shown to encode distinct aspects of the visual scene (9, 11, 23, 26, 67) and to receive separate sets of inputs from the retina (21). This suggests a tight link between the visual information that is encoded in a particular output circuit of the superior colliculus and the type of behavior this circuit triggers. The two inhibitory output pathways of the colliculus investigated here likely have a modulatory rather than an initiating role in behavior. We found that each population of Gad2 neurons, independent of their projection target, encodes similar visual features and receives a similar set
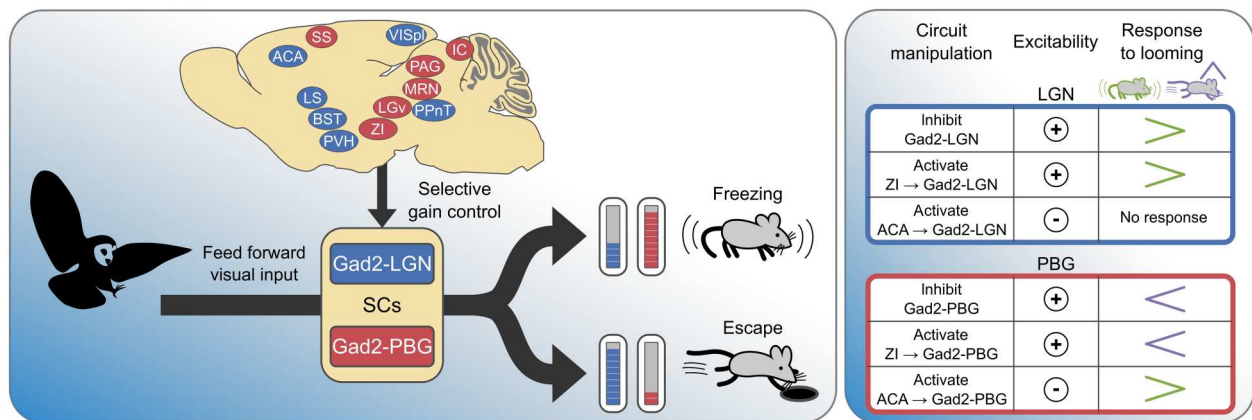
Fig. 9. Summary: Selective sampling of brain-wide inputs by LGN- and PBG-projecting Gad2 cells regulates routing of feedforward visual information and responses to visual threat. (**Left**) Circuit architecture that allows for flexible behavioral responses to a looming stimulus. (**Right**) Effects of circuit manipulations on looming evoked innate responses.

of inputs from the retina. Hence, contrary to descriptions of other output circuits of the colliculus, it appears that for Gad2 neurons, it is not the type of visual threat that favors activation of one circuit over the other. Instead, we found strong biases in the non-retinal inputs to Gad2 neurons and circuit-specific modulation by locomotion. This suggests that the balance of activation between each Gad2 output circuit, and the resulting behavior, is mediated by information about the animal's activity, internal state, or surroundings.

The brain-wide inputs to the superior colliculus have been extensively documented in mice and other small rodents (28, 31). Almost all cortical areas that we found to innervate Gad2 neurons are known to provide input to the superior colliculus. This includes several visual cortical areas and the retrosplenial cortex (28, 68), ACA, the auditory (AUD) and motor cortex (MOs), somatosensory cortices (SSp and SSs), orbital (ORB) and temporal association areas (TEa), and ILA and prelimbic (PL) areas (28). Similarly, many of the MB areas found in this study have been previously shown to innervate the superior colliculus, i.e., PPN, PAG, APN, CUN, SNr, and IC (28).

These results hold very well for the inputs to the Gad2-PBG circuit, where only 3 of the 21 PBG-biased areas have not been previously described in mice (PCGSG, MRN, and CENT). However, in the Gad2-LGN circuit, 17 of the 28 Gad2-LGN-biased inputs have not been previously described. Most of those areas are hypothalamic nuclei [PeVH, medial mammillary nucleus (MM), PVH, lateral preoptic area (LPO), preoptic nuclei, anterior hypothalamic nucleus, and dorsal hypothalamic nucleus], but also include parts of the striatum (LSv, LSd, and MEA), TH (PPnT and VPM), MB (anterior and ventral tegmental nucleus and red nucleus), and some other nuclei (BST, dorsal peduncular area, and prosubiculum). In addition, of the 20 balanced inputs to Gad2 neurons, seven nuclei have not previously been reported to provide input to the superior colliculus in mice, accessory oculomotor nuclei, medial vestibular nucleus, nucleus of the optic tract, central amygdala, posterior hypothalamic nucleus, premammilary nucleus, and PPT (28, 31, 69, 70). Together, we identified a number of non-cortical input areas that have not previously been described.

There are two likely reasons why we identified regions not previously reported to provide input to the colliculus. First, each study used different tools to label the inputs to the superior colliculus. For example, Benavidez et al. (28) combined anterograde tracing, with AAVs and dye injections, into mostly cortical areas with retrograde tracing using cholera toxin-B. Only a few projections were investigated using rabies viral vectors. Because of the high transfection efficiency of the CVS variant of rabies vectors used here, we might have labeled sparse, previously unobserved input regions such as the MM and LPO. A recent rabies tracing study has claimed to also identify previously unknown connections due to increased transmission efficiency of the CVS strain (71). Second, different methods were used to identify input areas. While we counted cell bodies, Benavidez et al. (28) analyzed fluorescence intensity, which, for sparsely labeled areas, might not cross the detection threshold. Together, we found a strong overlap with previously identified cortical inputs to the superior colliculus while also identifying previously unidentified, subcortical input regions using an efficient rabies-based transsynaptic tracing approach.

Retrograde transsynaptic labeling of retinal and brain-wide inputs

To target the retinal and brain-wide inputs to the colliculus, we applied a rabies virus-based transsynaptic strategy where a Cre-dependent helper virus expressing the receptor TVA and rabies-G was injected into one of the targets of Gad2 neurons. Subsequently, an EnvA-coated rabies virus was injected into the superficial layers of the superior colliculus to specifically target the LGN- or PBG-projecting Gad2 cells. We have previously shown that our helper virus has no leakage in Cre-negative animals (21). To decrease neuronal toxicity and increase transduction efficiency, we used the CVS-N2c rabies strain in addition to the SAD-B19 strain (72, 73). When comparing the data obtained with the two strains, we found similar relative infection rates for individual brain areas innervating Gad2-LGN or Gad2-PBG (fig. S5C). However, in general, experiments using the CVS-N2c strain showed a selective increased efficiency in transfecting the CTX compared to experiments using the SAD-B19 strain. While this will not affect the comparison of the inputs from any single area to the two Gad2 populations, it does affect the relative percentages and densities among different areas and needs to be taken into account when comparing the results reported here to other studies of inputs to the colliculus.

The quality of the labeling of inputs depends on a combination of injection precision and the chance of labeling nearby axonal projections to off-target areas. The PBG is not in close proximity to other targets of Gad2 neurons, and hence, the risk of infecting non-PBG–projecting neurons with the helper virus is small. In the case of the LGN, we targeted the dorsal part, but due to the close proximity we obtained labeling of axons projecting to both the ventral and dorsal LGN, which both receive inputs from the superior colliculus (23, 43, 74). We found labeled Gad2 neurons in the superficial layers of the SCs after retrograde labeling from both the PBG and LGN (Fig. 3 and fig. S4D).

To limit our investigation to the SCs, we performed depth limited injections of AAV and rabies virus. This resulted in the labeling of neurons that were primarily limited to the SCs for our two-photon imaging (Figs. 3 and 6), chemogenetic manipulation (Fig. 7 and S7), and rabies tracing experiments (fig. S4). In our rabies tracing experiments, we found that the vast majority of starter cells in our experiments were indeed in the SCs (83%), but some putative starter neurons (17%) were also found in the intermediate SC, predominantly located close to the border of the SCs in the SCig (fig. S4). Some of the inputs that we describe here, in particular the sparsely labeled inputs, might be a consequence of labeling starter neurons below the SCs, likely in the SCig. In summary, the combination of the *Gad2-Cre* mouse line with local injection of a helper virus and highly efficient rabies viral vectors allowed us to confidently identify the inputs to Gad2 neurons in the colliculus.

What role projections from the colliculus to the LGN have in guiding innate behaviors or whether direct projections from the retina to the visual TH play a role in avoiding danger remains unclear. Here, we found reliable changes in visually guided reactions to threat when manipulating Gad2-LGN projections, suggesting that projections to the LGN do influence visually guided behavior. As we also found Gad2 projections in the LP, it remains to be determined whether these LP projections are collaterals of LGN-projecting Gad2 neurons or an independent set of projections from neurons in the SCs or SCig.

Modulation of behavior through circuit-specific non-retinal inputs

There is a strong relationship between the functional response properties of the Gad2-LGN and Gad2-PBG neural populations and the inputs they receive from across the brain (Figs. 5 and 6). We found that 51 brain areas provide preferential input to one of the two Gad2 inhibitory output pathway of the superior colliculus, creating a circuit architecture that enables the selective integration of broad sets of inputs (sensory, motor, state, memory, etc.). For example, we found that motor-related areas tend to innervate PBG-projecting Gad2 neurons, which, in turn, are more strongly modulated during locomotion, while LGN-projecting Gad2 cells receive more inputs from areas associated with cognitive functions. This organization suggests that information about self-motion has a larger impact on escape reactions, while knowledge about the environment and memories might exert a greater influence on arrest behavior.

How any specific input to Gad2 neurons modulates innate behaviors in a pathway-specific manner remains to be determined. We investigated the effect of two areas, the ZI and the ACA. The ZI is associated with a gating role between sensory stimuli and motor responses (75, 76) and is involved in auditory innate flight responses (77) and predatory hunting (78). The rodent ACA has been determined to have a critical role in regulating fear responses to learned threats (79–81) and in reducing innate freezing responses (82), while in primates, the ACA plays a role in mediating innate fear (83–85). Manipulations that increased the excitability of the LGN over the PBG (activation of Gad2-LGN–projecting putative GABAergic ZI neurons or activation of Gad2-PBG–projecting putative glutamatergic ACA neurons) led to the favoring of freezing over escaping behaviors. On the other hand, increasing the excitability of the PBG through activation of Gad2-PBG–projecting ZI neurons favored escape responses. These manipulation experiments resulted in changes to the balance of behaviors evoked by visual looming that were predicted by the input-output relationship of the circuit being activated.

However, there are a few caveats to our interpretation above. We observed that optogenetic activation of Gad2-LGN–projecting ACA neurons abolished most innate reactions to the presentation of overhead looming stimuli. This could be the result of ACA inputs being some of the most numerous inputs to Gad2 neurons (Fig. 4), suggesting that optogenetic stimulation might lead to enough excitatory drive of inhibitory neurons in the colliculus to eliminate visual triggering of behavior. Alternatively, ACA neurons innervating the Gad2-LGN circuit might have collaterals that innervate other collicular neurons or brain regions and hence influence behavior via more than one pathway. Within the superior colliculus, some neurons in the ZI and ACA could have collaterals innervating both the Gad2-LGN and Gad2-PBG circuit. This is unlikely as we found differences in the spatial distribution of input neurons, from both the ZI and ACA, to the two circuits (fig. S8), and activating circuit-specific ZI and ACA inputs to the superior colliculus resulted in a predictable impact on behavior based on their innervation biases and the effect of chemogenetic inhibition of the Gad2-LGN and Gad2-PBG pathways (Figs. 7 and 8F). In addition, the ACA and ZI neurons, retrogradely labeled from the dorsal superior colliculus, may have collaterals that project to deeper layers. While we predominantly labeled inputs to the retino-recipient layers of the superior colliculus (fig. S4D), it is known that most of the inputs from both the ACA and ZI innervate the intermediate and deep layers of the superior colliculus (28, 86). It is currently unknown to what extent inputs to distinct layers of the superior colliculus are carried by either different neurons or collaterals of the same neuron.

In summary, we uncover that different output circuits of the superior colliculus sample from distinct brain-wide networks, such that the feedforward transfer of visual information can be selectively adjusted to influence behavior. We suggest that this circuit structure allows the superior colliculus to selectively integrate a broad set of inputs (sensory, motor, brain state, and memory) to flexibly switch the relationship between sensory inputs and behavioral outputs. Specifically for the superior colliculus, the combination of circuit-specific sampling of inputs and segregated outputs provides the circuit infrastructure to support the flexible triggering of behavior in response to the same visual stimulus under different conditions. These results represent one circuit motif of theoretical work predicting that flexible input-output mappings require non-random connections among multiple subpopulations of neurons (87).

METHODS

Experimental design

This study investigates two populations of *Gad2*-positive neurons of the mouse superior colliculus (sensory-related part: SCzo, SCsg, and SCop) projecting to either the LGN or PBG (Gad2-LGN and Gad2-PBG neurons). In four parts, we looked at the intersection of the two populations, each population's response to visual stimuli and locomotion, their brain-wide inputs, and their involvement in innate defensive behavior. First, projection targets of *Gad2*-positive neurons of the SCs were confirmed and the intersection of both populations was investigated by *Cre*-dependent anterograde and retrograde tracing in the *Gad2-IRES-Cre* mouse line, respectively. Second, the neural responses were investigated by awake head-fixed two-photon calcium imaging of the retrogradely traced populations. Third, retrograde transsynaptic tracing allowed the identification of brain-wide inputs to the two circuits. Fourth, freely moving behavior experiments paired with either chemogenetic inhibition of Gad2-LGN or Gad2-PBG neurons, or optogenetic activation of each population's ZI or ACA inputs, while animals were presented with a visual threat, allowed investigating the contribution of these circuits on innate defensive behaviors. A list of mice, viruses, equipment, software, and resources used is provided in Table 1.

Mice

All experimental procedures were approved by the Ethical Committee for Animal Experimentation (ECD) of the KU Leuven and followed the European Communities Guidelines on the Care and Use of Laboratory Animals (014-2018/EEC, 165-2018/EEC, 166-2018/EEC). Both male and female adult (1 to 3 months old) transgenic *Gad2-IRES-Cre* mice (JAX: 10802) were used in our experiments (Table 1). Mice were kept on a 12-hour light-dark cycle (lights on at 7:00 a.m.), and sterilized food pellets and water were provided ad libitum.

Virus strategy

Labeling of SC Gad2 projections

Cre-dependent AAV (*AAV-flox-tdTomato-SypEGFP*) (50 nl) coding for tdTomato and GFP-tagged synaptophysin was unilaterally injected to the SC of *Gad2-Cre* mice.

Table 1. Resource table.

Reagent/Resource	Designation	Source or reference	Identifiers
Genetic reagent (*Mus musculus*)	Gad2-IRES-CRE mouse line	The Jackson Laboratory	JAX:10802
Antibody	Anti-GFP (chicken, polyclonal, 1:500)	Thermo Fisher Scientific	Catalog no. A-10262; RRID: AB_2534023
Antibody	Alexa 488 donkey anti-chicken 1:500	Jackson ImmunoResearch	Catalog no. 703-545-155; RRID: AB_2340375
Antibody	Anti-ChAT (goat, polyclonal, 1:200)	Millipore	Catalog no. AB144P; RRID: AB_11214092
Antibody	Alexa 633 donkey anti-goat 1:500	Thermo Fisher Scientific	Catalog no. A-21082; RRID: AB_10562400
Antibody	SMI32 (mouse, monoclonal, 1:1000)	BioLegend	Catalog no. 801701; RRID: AB_2564642
Antibody	Cy3 donkey anti-mouse (1:400)	Jackson ImmunoResearch	Catalog no. 715-165-151; RRID: AB_2315777
Antibody	Dylight 405 donkey anti-mouse	Thermo Fisher Scientific	Catalog no. A-48257; RRID: AB_2884884
Antibody	Dylight 405 donkey anti-mouse	Jackson ImmunoResearch	Catalog no. 715-475-150; RRID: AB_2340839
Antibody	Anti-CART (rabbit, polyclonal, 1:500)	Phoenix Pharmaceuticals	H-003-62; RRID: AB_2313614
Antibody	DyLight 405 donkey anti-rabbit 1:400	Jackson ImmunoResearch	Catalog no. 715-475-150; RRID: AB_2340839
Antibody	555 Donkey anti rabbit 1:500	Thermo Fisher Scientific	Catalog no. A-31570; RRID: AB 2313501
Antibody	FOXP2 (goat, polyclonal, 1:500)	abcam	Catalog no. 1307; RRID: AB_1268914
Antibody	Alexa 555 donkey anti-goat 1:300	abcam	Catalog no. ab150130
Antibody	Anti-RFP (rabbit, polyclonal, 1:1000)	Rockland	Catalog no. 600-401-379; RRID: AB_2209751
Antibody	DAPI (1:2000)	Roche	Catalog no. 10276236001
Tracer	Lipophilic tracers DiI, DiD, DiO	Thermo Fisher Scientific	Catalog nos. D7776, D7757, and D275
Virus	*EnvA-RVΔG-GCaMP6s: EnvA-coated SAD-B19-△G-GCaMP6s*	This paper is based on aliquots obtained from the Laboratory of Botond Roska/Karl-Klaus Conzelmann	N/A
Virus	*EnvA-RVΔG-GCaMP6f: EnvA-coated CVS-N2c-△G-GCaMP6f*	This paper is based on aliquots obtained from the Laboratory of Andy Murray	N/A
Virus	*EnvA-RVΔG-Chr2-YFP: EnvA-coated CVS-N2c-ΔG-Chr2-YFP*	This paper is based on aliquots obtained from the Laboratory of Andy Murray	N/A
Virus	*HSV-flox-GCaMP6s: HSV-hEF1α-LS1L-GCaMP6s*	R. Neve (MGH)	RN507
Virus	*HSV-flox-mCherry: HSV-hEF1α-LS1L-mCherry*	R. Neve (MGH)	RN413
Virus	*HSV-flox-TVA-G-mCherry (SAD): HSV-hEF1α-LS1L-TVA950-T2A-G-IRES-mCherry*	R. Neve (MGH)	RN716
Virus	*HSV-flox-TVA-G-mCherry (CVS): HSV-hEF1α-LS1L-TVA950-T2A-n2c(G)-IRES-mCherry*	R. Neve (MGH)	RN728
Virus	*HSV-flox-FLP-mCherry: HSV-hEF1α-LS1L-mCherry-IRES-flpo*	R. Neve (MGH)	RN422
Virus	*HSV-flox-FLP: HSV-hEF1α-LS1L-flpo*	R. Neve (MGH)	RN433
Virus	*AAV-flox-tdTomato-SypEGFP: AAV1-phSyn1(S)-FLEX-tdTomato-T2A-SypEGFP*	Addgene	No. 51509-AAV1
Virus	*AAV-flip-hM4Di-mCherry: AAV8.2-hEF1α-fDIO-hM4Di-mCherry-WPRE*	R. Neve (MGH)	RN10
Virus	*AAV-flip-GCaMP6s: AAV1-EF1α-fDIO-GCaMP6s*	Addgene	No. 105714
Virus	*AAV-mCherry: AAV2-CMV-mCherry*	Vector Biolabs	No. 7104

continued on next page

Reagent/ Resource	Designation	Source or reference	Identifiers
Chemicals, peptides, and recombinant proteins			
Reagent	10× PBS	VWR	Catalog no. 437117K
Reagent	1× PBS	VWR	Catalog no. 444057Y
Reagent	Histofix 4%	Roche	Catalog no. P087.5
Reagent	Normal donkey serum	Millipore	Catalog no. 30-100ML
Reagent	10% Bovine serum albumin	Sigma	Catalog no. SRE0036-250ML
Reagent	DMEM, high glucose	Thermo Fisher Scientific	Catalog no. 41965062
Reagent	Trypsin 0.05%	Thermo Fisher Scientific	Catalog no. 25300054
Reagent	Fetal bovine serum (FBS)	Thermo Fisher Scientific	Catalog no. 10270106
Reagent	2,2′-thiodiethanol (TDE)	Sigma	Catalog no. 166782-500G
Reagent	ProLong Gold Antifade Mounting Medium	Thermo Fisher Scientific	Catalog no. P36934
Chemical compound, drug	Sodium azide (NaN_3)	Sigma	Catalog no. S2002-100G
Chemical compound, drug	Triton X-100	Sigma	Catalog no. S8875
Chemical compound, drug	Clozapine N-oxide (CNO)	Sigma	C0832
Chemical compound, drug	Sodium chloride (NaCl)	Sigma	Catalog no. S7653-250G
Chemical compound, drug	Potassium chloride (KCl)	Sigma	Catalog no. P5405-25G
Chemical compound, drug	Calcium chloride ($CaCl_2$)	Sigma	Catalog no. C5670-100G
Chemical compound, drug	Magnesium chloride ($MgCl_2$)	Sigma	Catalog no. 4880
Chemical compound, drug	D-Glucose (Dextrose)	Sigma	Catalog no. D9434-250G
Chemical compound, drug	Sodium phosphate monobasic (NaH_2PO_4)	Sigma	Catalog no. S5011
Chemical compound, drug	Sodium hydroxide (NaOH)	Sigma	Catalog no. 655104-500G
Chemical compound, drug	Sodium bicarbonate ($NaHCO_3$)	Sigma	Catalog no. S8875-1KG
Cell lines	BHK cells	Laboratory of Botond Roska/Laboratory of Karl-Klaus Conzelmann	N/A
Cell lines	B7GG cells	Laboratory of Botond Roska/Laboratory of Karl-Klaus Conzelmann	N/A
Cell lines	BHK-EnvA cells	Laboratory of Botond Roska/Laboratory of Karl-Klaus Conzelmann	N/A
Cell lines	HEK293T-TVA cells	Laboratory of Botond Roska/Laboratory of Karl-Klaus Conzelmann	N/A
Cell lines	Neuro2a-G cells	Laboratory of Andy Murray	N/A
Cell lines	Neuro2a-EnvA cells	Laboratory of Andy Murray	N/A
Software and algorithms			
Software	Fiji	https://fiji.sc	RRID: SCR_002285
Software	MATLAB	Mathworks	RRID: SCR_001622
Software	Zen lite	Zeiss	
Software	ChAT band detector	This paper	https://github.com/farrowlab/ChATbandsDetection
Software	PYTHON 3.4	Python Software Foundation	www.python.org

continued on next page

Reagent/ Resource	Designation	Source or reference	Identifiers
Software	CalmAn 1.7.1	Flatiron Institute	https://github.com/flatironinstitute/ CalmAn (version 1.7.1. accessed 10 January 2020)
Software	GNU Octave	Free Software Foundation	www.gnu.org/software/octave
Software	Psychophysics Toolbox	Psychtoolbox	http://psychtoolbox.org
Software	WaveSurfer (version: 0.918)	Janelia Research Campus	http://wavesurfer.janelia.org/
Software	ScanImage	Former: Vidrio Technologies, now: MBF Bioscience	https://docs.scanimage.org/
Other			
Other	Rapid Flow Filters 0.2 µm pore size	VWR	Catalog no. 514-0027
Other	Wiretrol II capillary micropipettes	Drumond Scientific	Catalog no. 5-000-2005
Other	Borosilicate glass	Sutter Instrument	Catalog no. BF100-20-10
Other	Glass cylinders, Ø 3 mm		
Other	Round borosilicate cover glasses, Ø 3 mm, 0.1-mm thickness	Multichannel Systems	Catalog no. 640728
Other	UV-curing optical adhesive	Norland	61
Other	Metabond dental cement	Crown & Bridge	
Other	Super-Bond C&B kit for self-curing adhesive resin cement	Sun Medical	
Other	Laser-based micropipette puller	Sutter Instrument	Catalog no. P-2000
Other	Small animal stereotaxic workstation	Narishige	Catalog no. SR-5N
Other	Stereotaxic micromanipulator	Narishige	Catalog no. SM-15R
Other	Hydraulic oil micromanipulator	Narishige	Catalog no. MO-10
Other	Oil microinjector	Narishige	Catalog no. IM-9B
Other	Two-photon microscope	Scientifica	Serial no. 14200
Other	780 nm LED light source	Thorlabs	Catalog no. M780L3
Other	Patch-clamp amplifier	Molecular Device	Axon Multiclamp 700B
Other	Patch-clamp microscope	Scientifica	Slice Scope
Other	Patch-clamp manipulator	Scientifica	Serial no. 301311
Other	Zeiss LSM 710 confocal microscope	Zeiss	Catalog no. LSM710
Other	473 nm DPSS laser system	Laserglow Technologies	R471003GX
Other	Rotary joint splitter	Thorlabs	RJ2, 400–700 nm, 50:50 Split
Other	FC/PC to Ø1.25 mm Ferrule Patch Cable	Thorlabs	M83L01 - Ø200 µm Core
Other	FC/PC-FC/PC fiber patch cable	Thorlabs	M72L02
Other	Fiber optic cannula—3.5 mm	Doric LENSES	B280-2304-3.5
Other	Fiber optic cannula—5 mm	Thorlabs	CFMLC12L05

Labeling of LGN- or PBG-projecting Gad2 cells
Cre-dependent HSV (200–400 nl) coding for different fluorescent proteins was unilaterally injected to the LGN (*HSV-flox-GCaMP6s*) and the PBG (*HSV-flox-mCherry*) of *Gad2-Cre* mice.

In vivo two-photon imaging of LGN- and PBG-projecting Gad2 cells
We applied a double conditional strategy to independently target the two populations. First, a Cre-dependent HSV expressing flippase was unilaterally injected to either the LGN (300 nl of 3:2 mix of *HSV-flox-Flp* and *AAV-mCherry*) or PBG (300 nl of *HSV-flox-Flp-mCherry*) of 6-week-old *Gad2-Cre* mice. Two weeks later, 800 nl of Flp-dependent AAV expressing a fluorescent calcium sensor (*AAV-flip-GCaMP6s*) was injected in five to six different locations of the ipsilateral superior colliculus.

Chemogenetic inhibition of LGN- and PBG-projecting Gad2 cells
We applied a similar double conditional strategy as for in vivo two-photon imaging. *HSV-flox-Flp* (300 nl) was injected bilaterally to either the LGN or PBG of 6-week-old *Gad2-Cre* mice. Two weeks later, an *Flp*-dependent AAV expressing *hM4Di* (*AAV-flip-hM4Di-mCherry*) was bilaterally injected into the superior colliculus (600 nl in total per side, three to four locations per side).

Retrograde transsynaptic labeling of input neurons to LGN- or PBG-projecting Gad2 cells and retinal physiology

First, an HSV expressing G-protein and TVA in a Cre-dependent manner [*HSV-flox-TVA-G-mCherry* (SAD) or *HSV-flox-TVA-G-mCherry* (CVS)] was unilaterally injected to either the LGN or PBG of *Gad2-Cre* mice. Three weeks later, G-deleted rabies virus coated with envelope-A [*EnvA-RV(SAD)ΔG-GCaMP6s* or *EnvA-RV(CVS)ΔG-GCaMP6f*] was injected in the ipsilateral superior colliculus for cell tracing (600 nl total, 150 nl at four locations).

Optogenetic activation of input neurons to LGN- or PBG-projecting Gad2 cells

A retrograde transsynaptic labeling strategy was used to bilaterally express the light-gated ion channel channelrhodopsin-2 (ChR2) in input neurons to LGN- and PBG-projecting Gad2 cells. Here, 300 nl of *HSV-flox-TVA-G-mCherry* (CVS) was bilaterally injected to either the LGN or PBG of *Gad2-Cre* mice. Three weeks later, 600 nl (150 nl at four locations) of rabies virus expressing ChR2 (*EnvA-RV(CVS)ΔG-ChR2-YFP*) was injected into each side of the superior colliculus.

Stereotaxic surgery
General procedures

Animals were quickly anesthetized with isoflurane (Iso-vet 1000 mg/ml) and a mixture of ketamine and medetomidine [0.75 ml of ketamine (100 mg/ml) + 1 ml of medetomidine (1 mg/ml) + 8.2 ml of saline]. Mice were placed in a stereotaxic workstation (Narishige, SR-5N). We used micropipettes (Wiretrol II capillary micropipettes, Drumond Scientific, 5-000-2005) with an open tip of around 30 μm and an oil-based hydraulic micromanipulator MO-10 (Narishige) for virus injections. Dura tear (NOVARTIS, 288/28062-7) was applied to protect the eyes. To label the injection sites, DiD (Thermo, D7757) was used to coat the pipette tip. The injection coordinates for the LGN in a 4-week-old mouse with a bregma-lambda distance of 4.7 mm were as follows: AP: −2.06; ML: ±2.00; DV: 2.60 mm. The injection coordinates for PBG were as follows: AP: −4.20; ML: ±1.95; DV: 3.50 mm. AP positions were adjusted based on the bregma-lambda distance of each animal. To cover the whole superior colliculus, we injected virus at a depth of 1.7–1.8 mm at three to four different locations within a 1-mm^2 field anterior of lambda and starting at the midline. If no fiber or window was implanted, after injection, the wound was closed using Vetbond tissue adhesive (3M, 1469). After surgery, mice were allowed to recover on top of a heating pad and were provided with soft food and water containing antibiotics (emdotrim, ecuphar, BE-V235523).

Optic fiber implantation

A fiber optic cannula was implanted in the targeted input areas the same day as rabies virus injection in the superior colliculus. For ACA, dual (200-μm-diameter, 3.5-mm-long) cannulas (Doric LENSES) were stereotactically implanted (left hemisphere: AP: +1; ML: +0.5; DV: 1.25; right hemisphere: AP: +1.9; ML: −0.5; DV: 30° from the reference plane, 1.65 mm). For ZI, a 200-μm-diameter, 5-mm-long cannula (Thorlabs) was stereotactically implanted (AP: −2; ML: ±1.4; DV: 4.3).

Cranial window implantation

A cranial window was implanted above the superior colliculus on the same day as the AAV injection. A metal head post was fixated on the skull, and a circular 4-mm craniotomy was performed above the frontal two-thirds of the left superior colliculus (ML: 0.0 to 4.0 mm, AP: −0.7 to −4.7 mm). The brain above the colliculus was removed and a cannular window of 3-mm diameter and 4-mm height was implanted and fixated with dental cement (*88*).

Immunohistochemistry
Retina immunohistochemistry

Dissected retinas were fixed in 4% paraformaldehyde (PFA, Histo-fix, ROTH, P087.5 mm) with 100 mM sucrose for 30 min at 4°C, and washed overnight or longer at 4°C. After washing, retinas were transferred to wells containing 10, 20, and 30% sucrose solution and allowed to sink for a minimum of 30 min, 1 hour at room temperature, and overnight at 4°C, respectively. The next day, freeze-cracking was performed: Retinas were frozen on a slide fully covered with 30% sucrose for 5 min on dry ice. The slides were then thawed at room temperature. The freeze-thaw cycle was repeated three times. Retinas were washed 3 times for 10 min each in 1× phosphate-buffered saline (PBS), followed by incubation with blocking buffer [10% Normal Donkey Serum (NDS), 1% bovine serum albumin (BSA), 0.5% Triton X-100, and 0.02% NaN$_3$ in 1× PBS] for at least 1 hour at room temperature or overnight. Both primary antibodies and secondary antibodies were diluted with 3% NDS, 1% BSA, 0.5% Triton X-100, and 0.02% NaN$_3$ in 1× PBS. Retinas were firstly incubated with primary antibody solution for 5 to 7 days under constant gentle shaking at room temperature. Then, retinas were washed three times, 15 min each, in 1× PBS with 0.5% Triton X-100 before being transferred into the secondary antibody solution. Primary antibodies used were chicken anti-GFP (Invitrogen, A-10262, 1:500), goat anti-ChAT (Chemicon, Ab144P, 1:200), mouse SMI32 (BioLegend, 801701, 1:1000), rabbit anti-CART (Phoenix, H-003-62, 1:500), and goat anti-FOXP2 (abcam, 1307, 1:2000). Secondary antibodies were Alexa488 donkey anti-chicken (Jackson ImmunoResearch, 703-545-155, 1:500), Alexa 633 donkey anti-goat (Invitrogen, A-21082, 1:500), Cy3 donkey anti-mouse (Jackson ImmunoResearch, 715-165-151, 1:400), and DyLight 405 donkey anti-rabbit (Jackson ImmunoResearch, 715-475-150, 1:200). Retinas were covered with mounting medium and a glass coverslip.

Brain immunohistochemistry

Extracted brains (after perfusion or without perfusion) were post-fixed in 4% PFA overnight at 4°C. Vibratome coronal or sagittal sections (200 μm) were collected in 1× PBS and were incubated in blocking buffer (1× PBS, 0.3% Triton X-100, and 10% Donkey serum) at room temperature for at least 1 hour or overnight. Then brain slices were incubated with primary antibodies solution for 2 to 3 days at 4°C with shaking. Slices were later washed three times for 10 min each in 1× PBS with 0.3% Triton X-100 and incubated in secondary antibody solution for at 4°C. Primary antibodies used were chicken anti-GFP (1:1000) and rabbit anti-mCherry (1:1500); secondary antibodies used were Alexa488 donkey anti-chicken (1:800) and 555 goat anti-rabbit (1:1000). Nuclei were stained with DAPI (4′,6-diamidino-2-phenylindole) (1:1000) or Nissl (NeuronTrace 435/455, Thermo, N21479, 1:150) together with the secondary antibody solution. Sections were then again washed three times for 10 min in 1× PBS with 0.3% Triton X-100 and one time in 1× PBS, covered with mounting medium and a glass coverslip. PBS was prepared with 0.02% NaN$_3$.

Confocal microscopy

Confocal microscopy was performed on a Zeiss LSM 710 microscope. Overview images of the retina and brain were obtained with a 10× [plan-APOCHROMAT 0.45 NA (numerical aperture), Zeiss] objective. The following settings were used for imaging the whole-mount retina: zoom 0.7, 4 × 4 tiles with 0% to 15% overlap, 2.37 μm/pixel resolution. For single retinal ganglion cell scanning, we used a 63× (plan-APOCHROMAT 1.4 NA, Zeiss) objective. The following settings were used: zoom 0.7, 2 × 2 tiles or more (depending on size and number of cells) with 0% to 15% overlap. This resulted in an *XY*-resolution of 0.38 μm/pixel and a *Z*-resolution between 0.25 and 0.35 μm/pixel. The z-stacks covered approximately 50 μm in depth. The whole-brain images were acquired with the 10× objective with zoom 0.7, multiple tiles with 5% to 15% overlap, and a z-stack of 20 μm. To determine the axon bouton density in the visual TH and PBG, high-resolution z-stacks (0.24×0.24 μm^2/pixel with 10 z-steps of 5 μm) of the cytosol and synaptophysin labeling were obtained with a 10× (plan-APOCHROMAT 0.45 NA, Zeiss) objective. The maximum projection of the z-stack was used for further analysis.

Ex vivo retinal recording

Retina preparation

Mice were dark-adapted for a minimum of 30 min. After cervical dislocation, eyes were gently touched with a soldering iron (Weller, BP650) to label the nasal part of the cornea and then enucleated. Retina isolation was done under deep red illumination in Ringer's medium (110 mM NaCl, 2.5 mM KCl, 1 mM CaCl$_2$, 1.6 mM MgCl$_2$, 10 mM D-glucose, and 22 mM NaHCO$_3$, bubbled with 5% CO$_2$/95% O$_2$, pH 7.4). The retinas were then mounted ganglion cell side up on filter paper (Millipore, HAWP01300) that had a 3.5-mm-wide rectangular aperture in the center, and superfused with Ringer's medium at 32° to 36°C in the microscope chamber for the duration of the experiment.

Retina recording

Fluorescent cells expressing *GCaMP6s* were targeted for recording using a two-photon microscope (Scientifica) equipped with a Mai Tai HP two-photon laser (Spectra Physics) at 920 nm wavelength. To facilitate targeting, two-photon fluorescent images were overlaid with the IR image acquired through a charge-coupled device camera. Infrared light was produced using the light from a light-emitting diode (LED). For some cells, z-stacks were acquired using ScanImage (Vidrio Technologies). Imaging frames were of 230×57 μm^2, sampled at 6.8 Hz (bidirectional scanning) and 512 × 128 pixel resolution. A selection of labeled retinal ganglion cells were recorded with two-photon imaging and patch clamp following the same procedure as in Reinhard *et al.* (*21*).

Presentation of visual stimuli

Stimuli were generated with an LCD projector (Samsung, SP F10M) at a refresh rate of 60 Hz, controlled with custom software written in Octave based on Psychtoolbox. The projector produced a light spectrum that ranged from ~430 to ~670 nm. The power produced by the projector was 300 lux (at full brightness blue screen and with short pass filter) at the retina. A combination of a neutral density filter and a short pass filter (cutoff wavelength = 475 nm) was used to control the stimulus intensity in logarithmic steps. Recordings were performed with filters decreasing the stimulus intensity by 1−2 log units. The following visual stimuli were used for retinal recordings:

Full-field (600×800 μm): The "chirp" stimuli started with slow transitions of black-white-black-gray, followed by two sinusoidal intensity modulations: a temporal modulation between black and white starting at 0.5 Hz and increasing to 8 Hz over a time of 8 s and a contrast modulation from 0 to 100% over a time period of 8 s at 2 Hz. The stimulus was repeated five times (*89*).

Expansion: A black disk linearly expanded from 2° to 50° with a speed of 150°/s at the center of a gray screen. The stimulus was repeated four times.

Dimming: A disk of 50° diameter linearly dimmed from background gray to black with a speed of 150°/s. The stimulus was repeated four times.

Moving bar: A white bar (0.3×1 mm) moved with a speed of 1 mm/s across the screen in eight directions (0°, 45°, 90°, 135°, 180°, 225°, 270°, and 315°). Each direction was repeated four times. The directions were randomized.

Looming: A black disk non-linearly expanded from 2° to 50° diameter with different speeds (8.3°/s, 83°/s, 166°/s, and 332°/s) at the center of a gray screen. Each condition was repeated four times.

In vivo two-photon imaging of the superior colliculus

The populations of LGN- and PBG-projecting Gad2 cells were independently labeled with a fluorescent calcium indicator by virus injections (see the "Virus strategy" section). Visual responses were recorded by two-photon calcium imaging through a cranial window in head-fixed, awake mice. Four mice were recorded for each projection target.

In vivo imaging sessions

A commercial two-photon galvo-resonance scanning microscope with a rotating arm (Thorlabs Multiphoton Microscope, B-Scope) was used to image the calcium signals of Gad2 neurons in the superficial layers of the superior colliculus. Neurons were imaged simultaneously at four equidistant planes separated by 30 to 50 μm, starting at 0 to 100 μm from the surface of the colliculus, reaching down to a maximum of 300 μm. A piezo-electric linear actuator (P-665, Physik Instrumente) moved the objective (Nikon 16x, 0.8 NA) in depth. Imaging frames were of 500 μm by 500 μm, sampled at 7.5 Hz (bidirectional scanning) and 512 × 512 pixels resolution. *GCaMP6s* was excited with a laser at 920-nm wavelength (Mai Tai DeepSee, Spectra Physics). A Pockel's cell was used to shut down the laser during flyback and to adjust its power by imaging depth to nominal powers of 30 to 90 mW at the end of the objective.

The head-fixed animals were free to run on a custom 3D-printed air-cushioned spherical treadmill (polystyrene white ball Ø 20 cm). We recorded the movement of the ball using two motion sensors (Tindie, PMW3360) with an analog readout of the pitch of the ball in direction of the animal's head. Eye movements of the mice were estimated by recording the left eye (ipsilateral to SC) with a lateral camera (Allied vision, mako G-030B + Lens: NAVITAR, HR F1.4/25MM) positioned at 25-cm distance.

The microscope was controlled, and the imaging frames were acquired using ScanImage 5.4. Running speed and trigger signals of stimulus beginning and end, two-photon imaging frames, and camera frames were recorded in WaveSurfer 0.97, yoked to ScanImage.

Before the first recording session, mice were habituated to human handling for 3 days. Then, they were head-fixed on the air-cushioned spherical treadmill for 5 min on the first day, with

increasing durations of 10 min, 30 min, and 1 hour in consecutive days. Animals usually adapted easily to running on the treadmill.

Presentation of visual stimuli

Stimuli were presented in grayscale on a curved LCD monitor (Samsung S32E590C, 729×425 mm^2, 2.9 cd/cm^2 mean luminance, 60 Hz refresh rate), controlled by custom software written in Octave using the Psychtoolbox. The monitor was at 30 cm distance and covered a visual field of 100° azimuth and 70° altitude on the right side of the mouse (contralateral to SC). The irradiance at the position of the mouse ranged from 0.15 to 30 lux (black to white screen); gray values were gamma corrected to yield a linearly perceived change in brightness.

The following visual stimuli were shown to the animal (white, gray, and black correspond to 100, 0, and −100% Weber contrast). A transistor-to-transistor logic (TTL) pulse was sent at the beginning and the end of each repeat for later alignment.

Expansion: A black or white disk linearly expanded from 2° to 50° within 0.95 s at the center of a gray or black screen, respectively. The stimulus was repeated 10 times, interleaved by 3 s of gray screen.

Shrinkage: A black disk linearly shrunk from 50° to 2° diameter within 0.95 s at the center of a gray screen. The stimulus was repeated 10 times, interleaved by 3 s of gray screen.

Dimming: A disk of 50° diameter linearly dimmed from background gray to black within 0.95 s at the center of the screen. The stimulus was repeated 10 times, interleaved by 3 s of gray screen.

Moving bar: A black bar of 8° width and extended till the edge of the screen moved perpendicular to its orientation in eight directions (0°, 45°, 90°, 135°, 180°, 225°, 270°, and 315°) with a speed of 40°/s across the screen. Each direction was repeated four times. The directions were randomized and interleaved by 3 s of gray screen.

Looming: A black disk expanded from 2° to 50° diameter at the center of a gray screen as if an object was approaching with linear speed with different size-to-speed ratios (10, 20, 40, and 80 ms). Each condition was repeated four times in random order and interleaved by 3 s of gray screen.

Moving spots: A black or white disk of different diameters (2°, 8°, and 32°) moved with 30°/s and 160°/s in two directions (left to right and right to left) across the center of a gray or black screen, respectively. Each combination of direction, size, and speed was repeated three times in random order and interleaved by 3 s of gray screen.

Band-pass noise: A patch of 50° was shown for 2 s on gray background with band-pass–filtered spatiotemporal white-noise patterns of different temporal (0.5, 1, 2, 4, and 8 Hz) and spatial cutoff frequencies (0.02, 0.04, 0.08, 0.16, and 0.32 cycles/°). Each pattern was randomly generated, and each condition was repeated four times in random order, interleaved by 3 s of gray screen.

Behavioral tests

All chemogenetic behavioral experiments were performed in a custom-made wooden box (W: 80 cm by L: 34 cm by H: 50 cm) with the display monitor positioned above the arena to show the visual stimuli. The light level, without extra light and with the monitor on, was 300 lux. Behavior was recorded at 30 fps using a camera positioned below the center of the arena. On the test day, intraperitoneal administration of clozapine metabolite clozapine-N-oxide (CNO, 2 mg/kg) or saline was used to activate hM4Di 30 min before the behavioral experiment. Mice were then allowed to explore the arena for at least 5 min. Looming and sweeping

stimuli were randomly shown. The number of trials depends on the mice's habituation time (when the mice stop to react to the visual stimuli). The chemogenetic experiment lasted no longer than 90 min.

Optogenetic manipulation

All experiments were performed in the same arena but with a width of 20 cm. A neutral density filter was applied to achieve a dim ambient light level of 0.3 lux to avoid the quick habituation to the looming stimulus. We used a 473-nm DPSS laser system (Laserglow Technologies, R471003GX) connected to a patchcord (Thorlabs, M72L02) with a rotatory joint splitter (Thorlabs, RJ2, 50:50 Split). Optogenetic stimulation was controlled with custom software written in MATLAB. The output laser power of each patch cable was measured at the tip of the fiber during stimuli of 20 Hz or 50 Hz (2 ms pulse width) and set at 2.0–2.5 mW. Both 20-Hz and 50-Hz conditions were used for each mouse, resulting in similar behavioral outputs. Optic fibers were implanted above the targeted areas. For ACA, we used the optic fiber with 3.5 mm length, 200 μm diameter, and NA = 0.37 (Doric Lenses, B280-2304-3.5); for ZI, we used the optic fiber with 5 mm length, 200 μm diameter, and NA = 0.39 (Thorlabs, CFMLC12L05). One day before the optogenetic test, mice were habituated to the patchcord. On the test day, mice were allowed to explore the arena for at least 5 min. Optogenetic stimulation was triggered when the mice moved away from the shelter and lasted for 20 s. The looming stimulus was triggered when the mice moved toward the danger zone. Both were done manually. Light stimulation was initiated at least 1 s before the visual stimulus and did not necessarily cover the full visual stimulation time.

Analysis of Gad2 projections

Quantification of the axon bouton density of Gad2 cells in the LP, LGd, LGv, and PBG was performed in two steps. First, the respective regions were marked and overlaid in the confocal images of the visual TH and PBG using ImageJ. As a reference, control regions (PO, PoT, and VPM) were marked in the same image where no labeling was expected. Second, the two-color channels for cytosol and axon bouton labeling were multiplied and median-filtered with a width of 3 pixels such that axon boutons were clearly visible circular patches. The labeled area was then determined as the percent area occupied by these patches with respect to the total area of each region. Peak densities were determined within manually picked regions of 50×50 μm^2 with highest bouton density. Statistically significant differences to the control regions were determined using a Kruskal-Wallis test.

Analysis of Gad2 cell labeling

Quantification of the overlapping percentage between neurons labeled from the HSV injection in LGN and PBG is based on 26 brain sections from four mice (Fig. 2D and table S1). One-way analysis of variance (ANOVA) was performed to compare the means of each group's percentage. The P values were further adjusted using a conservative Bonferroni correction method (90). The co-labeled cells have a significantly lower percentage of labeled cells than either LGN- or PBG-projecting Gad2 cells ($P < 0.001$). Quantification of the overlapping percentage between neurons labeled from the HSV injection in one area (control group) is based on 16 brain sections from three mice (fig. S1D and table S1). One-way

ANOVA and multiple comparisons were performed to compare the means of each group's percentage. The P values were further adjusted using the conservative Bonferroni correction method. Coordinates of labeled cells were extracted by registering a sequence of brain slices containing the superior colliculus (LGN group: 49 sections from seven mice; PBG group: 28 sections from four mice) to the Allen Brain Atlas (*45*).

Analysis of behavioral data

The animal's position was tracked using DeepLabCut software (*62*). Tracking data (e.g., nose, head, body, paw, and tail) were further thresholded and analyzed using custom-made MATLAB scripts. Frames with probability lower than 0.95 were filtered out and linearly interpolated. Position data were smoothed with a median filter of window size 5. Here, we used the middle of the body position to calculate the speed and track the movement. The behavioral responses were classified into one of the categories: escape, freeze, pauses, rearing, and no response based on their speed. For a better visualization of the balance of escape versus freeze behavior, we combined pauses, rearing, and no response together in the category of "others." An escape response is defined as periods of time during which the mouse speed was higher than 40 cm/s and the animal was directed to the refuge after the onset of this movement. A freeze response is a response with a very low baseline (<2 cm/s) or no movements for at least 2 s. All the behavioral classification in this study was automatically scored and confirmed by manual scoring.

Analysis of brain-wide input data

The divisions of brain regions and areas were based on the Allen Brain Atlas with some modifications as described previously (*10*). In detail, the whole brain was divided into eight parental regions including CTX (consisting of the isocortex and olfactory areas), cortical subplate (sCTX, consisting of the sCTX and cerebral nuclei), hippocampal formation, TH, HYP, MB, HB, and the 259 subareas thereof. Data S1 shows a full list of all areas. The rabies-labeled input neurons (expressing *GCaMP6* only) were manually labeled throughout the z-stack using the multi-point tool of ImageJ. Each section with the indicated input neurons was then matched to the standard Allen Mouse Brain Atlas using Allen CCF SHARP-Track toolbox (https://github.com/cortex-lab/allenCCF) (*45*). All detected *GCaMP6*-expressing cells in SCs were excluded from all statistical analysis, to ensure no starter cells (co-expressing *GCaMP6* and TVA-mCherry) were counted as input cells. The raw data output containing the coordinates of each labeled neuron is available in data S2. Areas with less than two counted cells were excluded in the analysis. Cell density was calculated as total cell number per area volume. Areas with less than six cells/mm³ [e.g., one cell in triangular nucleus of septum (area volume = 0.17 mm³)] and less than 0.2% of the total inputs were considered below background threshold and set to zero.

The bias index per brain area as calculated from the counted number of neurons N and brain area volume V is as follows.

$$\text{Cell density } \rho_{\text{brain area}} = \text{mean}[(N_{\text{brain area}}/V_{\text{brain area}})/(N_{\text{SCs+i}}/V_{\text{SCs+i}})]_{\text{all brains}}$$

$$\text{Cell percentage } P_{\text{brain area}} = \text{mean}[N_{\text{brain area}}/(N_{\text{total}} - N_{\text{SCs+i}})]_{\text{all brains}}$$

$$\text{Bias index}_{\text{brain area}} = \log_2[P_{\text{brain area}}(\text{Gad2} - \text{PBG})/P_{\text{brain area}}(\text{Gad2} - \text{LGN})]$$

The normalization was performed relative to the total number of input neurons in the whole brain/a certain parental region.

Threshold for biased input areas

To determine a threshold for significantly biased brain areas, for each brain, we randomly distributed the corresponding number of counted neurons (without SCs/i; Gad2-LGN: 38,300, 27,313, and 14,188 neurons, Gad2-PBG: 8948, 35,129, and 28,472 neurons) across all 69 labeled brain areas weighted by volume. We then calculated the bias index of each brain area for the shuffled brains in the same way as for the real brains. We calculated the 95% confidence interval of each brain area from 10,000 shuffles and calculated the mean confidence interval across brain areas, resulting in $\text{CI}_{\text{bias index}} = [-0.3, 0.3]$.

Analysis of ex vivo calcium imaging data

Two-photon imaging frames were registered, and regions of interest (ROIs) were determined using Suite2p (*91*) in Python 3.8. The time scale of the *GCaMP6f* used for deconvolution kernel is 0.7 s. The sampling rate per plane is 6.91 Hz. Thresholding scaling was set at 1 to extract ROIs. Resulting ROIs were manually curated by overlaying the ROIs with a maximum projection of the registered imaging frames, excluding the "non-cells." The resulting deconvolved traces of these selected ROIs were used for further analysis (Fig. 3J). Normalization was based on the maximum response crossing trials. For some of the simultaneously recorded retina ganglion cells, we also extracted the denoised traces of $\Delta F/F$ values for comparing with the patch-clamp spikes (fig. S3). Analysis of patch-clamp recordings used the same procedure as in Reinhard *et al.* (*21*). The repeats of visual stimuli and retinal responses were aligned using recorded stimulus start and frame triggers.

Direction and orientation selectivity

The direction and orientation selectivity of retinal ganglion cells were analyzed by calculating the direction selectivity index (DSI), orientation selectivity index (OSI), preferred directions, and preferred orientations from mean peak responses r_θ to each direction θ of the moving bar stimulus

$$\text{DSI} = \frac{|\Sigma_\theta r_\theta e^{i\theta}|}{\Sigma_\theta r_\theta}, \text{ preferred direction} = \text{angle}\left(\Sigma_\theta r_\theta e^{i\theta}\right)$$

$$\text{OSI} = \frac{|\Sigma_\theta r_\theta e^{2i\theta}|}{\Sigma_\theta r_\theta}, \text{ preferred orientation} = \text{angle}\left(\Sigma_\theta r_\theta e^{2i\theta}\right)/2$$

Neurons were considered direction or orientation selective when their DSI or OSI was larger than 0.2.

Analysis of retinal ganglion cell morphology
Extraction of dendritic parameters

The dendritic morphology of GFP-stained retinal ganglion cells was determined following the same procedure as in Reinhard *et al.* (*21*). Briefly, confocal z-stacks of individual ganglion cells of anti-ChAT– and anti-GFP–stained retinas were denoised, down-sampled, and binarized to extract the position of the On- and Off-ChAT bands using a custom deep learning framework and the position of the dendritic tree (anti-GFP). Z-stacks were warped to straighten the ChAT bands and a dendritic depth profile was determined from the number of bright pixels of the binarized GFP signal in the *Z*-direction. Dendritic tree diameters were calculated from the area of the convex hull of the dendritic tree in the *X-Y* plane as $D = 2^*(\text{area}/\pi)^{1/2}$.

Classification by dendritic morphology

The density of dendrites was plotted along the *Z*-axis. Each cell was classified as below, between, or above ChAT bands based on dendritic stratification depth. The bistratified cells were with dendritic density peaks aligned with the ChAT bands.

Quantification of SMI32+, CART+, and FOXP2+ retinal ganglion cells

Confocal image stacks of the anti-CART, SMI32, or anti-FOX2 and anti-GFP–stained retinas were opened in Fiji and the number of double-positive cells (CART/GFP, SMI32/GFP, or FOXP2/GFP) was counted by overlaying the two-color channels. Cells were marked using the point tool and counted manually using the cell counter plugin.

Analysis of in vivo calcium imaging data
Two-photon image registration and ROI extraction

Two-photon imaging frames were registered, and ROIs were determined using NNMF with CamAn 1.7.1 (Flatiron Institute) in Python 3.4. The signal decay time of the model was adjusted to *GCaMP6s* (1.4 s). Resulting ROIs were manually curated by overlaying the ROIs with a maximum projection of the registered imaging frames, selecting exclusively neural cell bodies. The resulting denoised traces of $\Delta F/F$ values of these selected ROIs were used for further analysis.

Peak responses and quality index

The repeats of visual stimuli and neural responses were aligned by using the simultaneously recorded stimulus start and imaging frame triggers. For each presented stimulus, a quality index and peak response of each ROI were calculated. The quality index was calculated from the variance of the brightness values C across time, $\text{var}(\cdot)_t$, and the mean across stimulus repeats, $\langle\cdot\rangle_r$, as follows:

$$QI = \frac{\text{var}(\langle C \rangle_r)_t}{\langle \text{var}(C)_t \rangle_r}$$

A neuron was considered visually responsive if the quality index for at least one of the stimuli was above 0.6. This includes 1496 of the 1883 recorded LGN-projecting and 199 of the 326 PBG-projecting Gad2 neurons.

Peak responses were calculated from the median stimulus response by taking the difference between the mean of the first 0.5 s before stimulus onset and the maximum during stimulus presentation. For each ROI, the median visual peak response across all stimuli was determined to estimate general visual response strength.

As Gad2-PBG neuron responses were generally much lower in amplitude than Gad2-LGN responses, we displayed boxplots of the normalized peak responses to each stimulus derived from dividing each peak response by the population median. We showed distributions of each population of visually responsive neurons by using boxplots. Whiskers extending to outliers until 1.5 of the interquartile range have been omitted for clarity in the main figure and can be reviewed in fig. S2B.

Direction and orientation selectivity

The direction and orientation selectivity of LGN- and PBG-projecting Gad2 neurons were analyzed by calculating the DSI, OSI, preferred directions, and preferred orientations from mean peak responses r_θ to each direction θ of the moving bar stimulus

$$DSI = \frac{|\Sigma_\theta r_\theta e^{i\theta}|}{\Sigma_\theta r_\theta}, \quad \text{preferred direction} = \text{angle}\left(\Sigma_\theta r_\theta e^{i\theta}\right)$$

$$OSI = \frac{|\Sigma_\theta r_\theta e^{2i\theta}|}{\Sigma_\theta r_\theta}, \quad \text{preferred orientation} = \text{angle}(\Sigma_\theta r_\theta e^{2i\theta})/2$$

Neurons were considered direction or orientation selective when their DSI or OSI was significantly larger (99% CI) than the index calculated from 10,000 shuffles, respectively.

Preferred spatiotemporal frequencies

Preferred spatiotemporal frequencies were determined from fitting a 2D Gaussian to the peak responses to the 5×5 combinations of the spatial and temporal frequencies of the band-pass noise stimulus (see above). The preferred frequency was then derived from the peak location of that fit. Because spatial and temporal frequencies increase by the power of two, this location has been determined in logarithmic coordinates.

Responses to running

The extent by which the responses of SC neurons are affected by running was estimated in two ways. First, we looked at how neurons responded to the onset of running. For this, time points of running onset were determined by threshold crossing throughout the entire recording session. We considered a running onset event when the animal ran faster than 3.5 cm/s while remaining still (speed <3.5 cm/s) for at least 5 s before the event.

Median running traces of each experiment and median cell response traces were calculated from 5 s before till 10 s after running onset. Normalized baseline-subtracted cell response traces were calculated by subtracting the mean response during the 5 s still period and dividing by the SD of that period.

Normalized baseline − subtracted response

$$= (\text{response} - \text{mean}[\text{response}]_{\text{still}})/\text{SD}[\text{response}]_{\text{still}}$$

The normalized baseline-subtracted responses were then grouped by their mean during running into up (>1 SD), down (<−1 SD), and non-modulated (between −1 and 1 SD).

We calculated the absolute responses to running by subtracting the neural activity during the still phase (fig. S6)

$$\text{Response to running} = \text{median}[\text{response}]_{\text{running}}$$
$$- \text{median}[\text{response}]_{\text{still}}$$

Visual responses and responses to running were then plotted together. For each group, we plotted the distributions of their absolute

response to running and tested significant differences between LGN- and PBG-projecting cells using a two-sample Kolmogorov-Smirnov test.

Second, we correlated the calcium responses of each neuron with the running speed of the entire recording session. The mean of the resulting Pearson correlation coefficients of LGN- and PBG-projecting Gad2 neurons was compared using a two-sided permutation t test. To test whether the distributions of correlations with running were significantly from chance level, correlation coefficients of each neuron were obtained from 10,000 random shifts of the running trace and a two-sample Kolmogorov-Smirnov test performed on the two distributions.

One- and two-dimensional distributions of median visual peak responses and median responses to running were estimated using the KDE() function of the matplotlib library in python with a Gaussian kernel of optimal width estimated by Scott's rule.

Statistical analysis
Statistical analyses are incorporated into each corresponding experimental section. The number of samples is indicated in figures, figure legends, and corresponding Results sections.

Supplementary Materials
This PDF file includes:
Figs. S1 to S9
Table S1
Legends for movies S1 and S2
Legends for data S1 and S2

Other Supplementary Material for this manuscript includes the following:
Movies S1 and S2
Data S1 and S2

REFERENCES AND NOTES
1. N. Tinbergen, *The study of instinct* (Clarendon Press, 1951).
2. D. Wei, V. Talwar, D. Lin, Neural circuits of social behaviors: Innate yet flexible. *Neuron* **109**, 1600–1620 (2021).
3. M. A. Basso, P. J. May, Circuits for action and cognition: A view from the superior colliculus. *Annu. Rev. Vis. Sci.* **3**, 197–226 (2017).
4. C. T. Gross, N. S. Canteras, The many paths to fear. *Nat. Rev. Neurosci.* **13**, 651–658 (2012).
5. Y. Lefler, D. Campagner, T. Branco, The role of the periaqueductal gray in escape behavior. *Curr. Opin. Neurobiol.* **60**, 115–121 (2020).
6. X. Liu, H. Huang, T. P. Snutch, P. Cao, L. Wang, F. Wang, The superior colliculus: Cell types, connectivity, and behavior. *Neurosci. Bull.* **38**, 1519–1540 (2022).
7. C. A. Duan, M. Pagan, A. T. Piet, C. D. Kopec, A. Akrami, A. J. Riordan, J. C. Erlich, C. D. Brody, Collicular circuits for flexible sensorimotor routing. *Nat. Neurosci.* **24**, 1110–1120 (2021).
8. D. A. Evans, A. V. Stempel, R. Vale, S. Ruehle, Y. Lefler, T. Branco, A synaptic threshold mechanism for computing escape decisions. *Nature* **558**, 590–594 (2018).
9. J. L. Hoy, H. I. Bishop, C. M. Niell, Defined cell types in superior colliculus make distinct contributions to prey capture behavior in the mouse. *Curr. Biol.* **29**, 4130–4138.e5 (2019).
10. A. Sans-Dublanc, A. Chrzanowska, K. Reinhard, D. Lemmon, B. Nuttin, T. Lambert, G. Montaldo, A. Urban, K. Farrow, Optogenetic fUSI for brain-wide mapping of neural activity mediating collicular-dependent behaviors. *Neuron* **109**, 1888–1905.e10 (2021).
11. C. Shang, Z. Liu, Z. Chen, Y. Shi, Q. Wang, S. Liu, D. Li, P. Cao, A parvalbumin-positive excitatory visual pathway to trigger fear responses in mice. *Science* **348**, 1472–1477 (2015).
12. C. Shang, Z. Chen, A. Liu, Y. Li, J. Zhang, B. Qu, F. Yan, Y. Zhang, W. Liu, Z. Liu, X. Guo, D. Li, Y. Wang, P. Cao, Divergent midbrain circuits orchestrate escape and freezing responses to looming stimuli in mice. *Nat. Commun.* **9**, 1232 (2018).
13. J. M. Ache, J. Polsky, S. Alghailani, R. Parekh, P. Breads, M. Y. Peek, D. D. Bock, C. R. von Reyn, G. M. Card, Neural basis for looming size and velocity encoding in the Drosophila giant fiber escape pathway. *Curr. Biol.* **29**, 1073–1081.e4 (2019).
14. G. De Franceschi, T. Vivattanasarn, A. B. Saleem, S. G. Solomon, Vision guides selection of freeze or flight defense strategies in mice. *Curr. Biol.* **26**, 2150–2154 (2016).
15. W. Schiff, J. A. Cavomess, J. J. Gibson, Persistent fear responses in rhesus monkeys to the optical stimulus of "looming". *Science* **136**, 982–983 (1962).
16. I. Temizer, J. C. Donovan, H. Baier, J. L. Semmelhack, A visual pathway for looming-evoked escape in larval zebrafish. *Curr. Biol.* **25**, 1823–1834 (2015).
17. M. Yilmaz, M. Meister, Rapid innate defensive responses of mice to looming visual stimuli. *Curr. Biol.* **23**, 2011–2015 (2013).
18. M. Yilmaz Balban, E. Cafaro, L. Saue-Fletcher, M. J. Washington, M. Bijanzadeh, A. M. Lee, E. F. Chang, A. D. Huberman, Human responses to visually evoked threat. *Curr. Biol.* **31**, 601–612.e3 (2021).
19. P. Dean, P. Redgrave, G. W. M. Westby, Event or emergency? Two response systems in the mammalian superior colliculus. *Trends Neurosci.* **12**, 137–147 (1989).
20. P. Wei, N. Liu, Z. Zhang, X. Liu, Y. Tang, X. He, B. Wu, Z. Zhou, Y. Liu, J. Li, Y. Zhang, X. Zhou, L. Xu, L. Chen, G. Bi, X. Hu, F. Xu, L. Wang, Processing of visually evoked innate fear by a non-canonical thalamic pathway. *Nat. Commun.* **6**, 6756 (2015).
21. K. Reinhard, C. Li, Q. Do, E. G. Burke, S. Heynderickx, K. Farrow, A projection specific logic to sampling visual inputs in mouse superior colliculus. *eLife* **8**, e50697 (2019).
22. X. Shi, J. Barchini, H. A. Ledesma, D. Koren, Y. Jin, X. Liu, W. Wei, J. Cang, Retinal origin of direction selectivity in the superior colliculus. *Nat. Neurosci.* **20**, 550–558 (2017).
23. S. D. Gale, G. J. Murphy, Distinct representation and distribution of visual information by specific cell types in mouse superficial superior colliculus. *J. Neurosci.* **34**, 13458–13471 (2014).
24. S. D. Gale, G. J. Murphy, Distinct cell types in the superficial superior colliculus project to the dorsal lateral geniculate and lateral posterior thalamic nuclei. *J. Neurophysiol.* **120**, 1286–1292 (2018).
25. Z. Xie, M. Wang, Z. Liu, C. Shang, C. Zhang, L. Sun, H. Gu, G. Ran, Q. Pei, Q. Ma, M. Huang, J. Zhang, R. Lin, Y. Zhou, J. Zhang, M. Luo, Q. Wu, P. Cao, X. Wang, Transcriptomic encoding of sensorimotor transformation in the midbrain. *eLife* **10**, e69825 (2021).
26. C. Bennett, S. D. Gale, M. E. Garrett, M. L. Newton, E. M. Callaway, G. J. Murphy, S. R. Olsen, Higher-order thalamic circuits channel parallel streams of visual information in mice. *Neuron* **102**, 477–492.e5 (2019).
27. K. H. Lee, A. Tran, Z. Turan, M. Meister, The sifting of visual information in the superior colliculus. *eLife* **9**, e50678 (2020).
28. N. L. Benavidez, M. S. Bienkowski, M. Zhu, L. H. Garcia, M. Fayzullina, L. Gao, I. Bowman, L. Gou, N. Khanjani, K. R. Cotter, L. Korobkova, M. Becerra, C. Cao, M. Y. Song, B. Zhang, S. Yamashita, A. J. Tugangui, B. Zingg, K. Rose, D. Lo, N. N. Foster, T. Boesen, H. S. Mun, S. Aquino, I. R. Wickersham, G. A. Ascoli, H. Hintiryan, H.-W. Dong, Organization of the inputs and outputs of the mouse superior colliculus. *Nat. Commun.* **12**, 4004 (2021).
29. E. Comoli, P. D. N. Favaro, N. Vautrelle, M. Leriche, P. G. Overton, P. Redgrave, Segregated anatomical input to sub-regions of the rodent superior colliculus associated with approach and defense. *Front. Neuroanat.* **6**, 9 (2012).
30. T. K. Doykos, J. I. Gilmer, A. L. Person, G. Felsen, Monosynaptic inputs to specific cell types of the intermediate and deep layers of the superior colliculus. *J. Comp. Neurol.* **528**, 2254–2268 (2020).
31. P. J. May, The mammalian superior colliculus: Laminar structure and connections. *Prog. Brain Res.* **151**, 321–378 (2006).
32. S. W. Oh, J. A. Harris, L. Ng, B. Winslow, N. Cain, S. Mihalas, Q. Wang, C. Lau, L. Kuan, A. M. Henry, M. T. Mortrud, B. Ouellette, T. N. Nguyen, S. A. Sorensen, C. R. Slaughterbeck, W. Wakeman, Y. Li, D. Feng, A. Ho, E. Nicholas, K. E. Hirokawa, P. Bohn, K. M. Joines, H. Peng, M. J. Hawrylycz, J. W. Phillips, J. G. Hohmann, P. Wohnoutka, C. R. Gerfen, C. Koch, A. Bernard, C. Dang, A. R. Jones, H. Zeng, A mesoscale connectome of the mouse brain. *Nature* **508**, 207–214 (2014).
33. F. Zhu, M. Cizeron, Z. Qiu, R. Benavides-Piccione, M. V. Kopanitsa, N. G. Skene, B. Koniaris, J. DeFelipe, E. Fransén, N. H. Komiyama, S. G. N. Grant, Architecture of the mouse brain synaptome. *Neuron* **99**, 781–799.e10 (2018).
34. K. Isa, K. Tokuoka, S. Ikeda, S. Karimi, K. Kobayashi, T. Sooksawate, T. Isa, Amygdala underlies the environment dependency of defense responses induced *via* superior colliculus. *Front. Neural Circuits* **15**, 768647 (2022).
35. J. Lee, B. L. Sabatini, Striatal indirect pathway mediates exploration via collicular competition. *Nature* **599**, 645–649 (2021).
36. Q. Montardy, Z. Zhou, L. Li, Q. Yang, Z. Lei, X. Feng, S. Chen, Q. Shi, H. Zhang, S. Chen, Z. Zhang, B. Zhao, F. Xu, Z. Lu, L. Wang, Dopamine modulates visual threat processing in the superior colliculus via D2 receptors. *iScience* **25**, 104388 (2022).
37. A. Fratzl, A. M. Koltchev, N. Vissers, Y. L. Tan, A. Marques-Smith, A. V. Stempel, T. Branco, S. B. Hofer, Flexible inhibitory control of visually evoked defensive behavior by the ventral lateral geniculate nucleus. *Neuron* **109**, 3810–3822.e9 (2021).
38. L. D. Salay, A. D. Huberman, Divergent outputs of the ventral lateral geniculate nucleus mediate visually evoked defensive behaviors. *Cell Rep.* **37**, 109792 (2021).

39. F. Hu, T. Kamigaki, Z. Zhang, S. Zhang, U. Dan, Y. Dan, Prefrontal corticotectal neurons enhance visual processing through the superior colliculus and pulvinar thalamus. *Neuron* **104**, 1141–1152.e4 (2019).

40. F. Liang, X. R. Xiong, B. Zingg, X.-Y. Ji, L. I. Zhang, H. W. Tao, Sensory cortical control of a visually induced arrest behavior via corticotectal projections. *Neuron* **86**, 755–767 (2015).

41. X. Zhao, M. Liu, J. Cang, Visual cortex modulates the magnitude but not the selectivity of looming-evoked responses in the superior colliculus of awake mice. *Neuron* **84**, 202–213 (2014).

42. M. Ahmadlou, L. S. Zweifel, J. A. Heimel, Functional modulation of primary visual cortex by the superior colliculus in the mouse. *Nat. Commun.* **9**, 3895 (2018).

43. K. L. Whyland, A. S. Slusarczyk, M. E. Bickford, GABAergic cell types in the superficial layers of the mouse superior colliculus. *J. Comp. Neurol.* **528**, 308–320 (2020).

44. H. Taniguchi, M. He, P. Wu, S. Kim, R. Paik, K. Sugino, D. Kvitsani, Y. Fu, J. Lu, Y. Lin, G. Miyoshi, Y. Shima, G. Fishell, S. B. Nelson, Z. J. Huang, A resource of Cre driver lines for genetic targeting of GABAergic neurons in cerebral cortex. *Neuron* **71**, 995–1013 (2011).

45. P. Shamash, M. Carandini, K. Harris, N. Steinmetz, A tool for analyzing electrode tracks from slice histology. bioRxiv 447995 [Preprint] 19 October 2018. https://doi.org/10.1101/447995.

46. L. R. Mangieri, Z. Jiang, Y. Lu, Y. Xu, R. M. Cassidy, N. Justice, Y. Xu, B. R. Arenkiel, Q. Tong, Defensive behaviors driven by a hypothalamic-ventral midbrain circuit. *eNeuro* **6**, ENEURO.0156-19.2019 (2019).

47. L. Wang, Z. Zhang, J. Chen, A. Manyande, R. Haddad, Q. Liu, F. Xu, Cell-type-specific whole-brain direct inputs to the anterior and posterior piriform cortex. *Front. Neural Circuits* **14**, 4 (2020).

48. C. A. Villalobos, M. A. Basso, Optogenetic activation of the inhibitory nigro-collicular circuit evokes contralateral orienting movements in mice. *Cell Rep.* **39**, 110699 (2022).

49. R. C. Almada, A. J. Genewsky, D. E. Heinz, P. M. Kaplick, N. C. Coimbra, C. T. Wotjak, Stimulation of the nigrotectal pathway at the level of the superior colliculus reduces threat recognition and causes a shift from avoidance to approach behavior. *Front. Neural Circuits* **12**, 36 (2018).

50. S. Hormigo, G. Vega-Flores, M. A. Castro-Alamancos, Basal ganglia output controls active avoidance behavior. *J. Neurosci.* **36**, 10274–10284 (2016).

51. H. Deng, X. Xiao, Z. Wang, Periaqueductal gray neuronal activities underlie different aspects of defensive behaviors. *J. Neurosci.* **36**, 7580–7588 (2016).

52. C. C. Crestani, F. H. Alves, F. V. Gomes, L. B. Resstel, F. M. Correa, J. P. Herman, Mechanisms in the bed nucleus of the stria terminalis involved in control of autonomic and neuroendocrine functions: A review. *Curr. Neuropharmacol.* **11**, 141–159 (2013).

53. A. V. Ferguson, K. J. Latchford, W. K. Samson, The paraventricular nucleus of the hypothalamus—A potential target for integrative treatment of autonomic dysfunction. *Expert Opin. Ther. Targets* **12**, 717–727 (2008).

54. S. Keshavarzi, R. K. P. Sullivan, D. J. Ianno, P. Sah, Functional properties and projections of neurons in the medial amygdala. *J. Neurosci.* **34**, 8699–8715 (2014).

55. Ç. Aydın, J. Couto, M. Giugliano, K. Farrow, V. Bonin, Locomotion modulates specific functional cell types in the mouse visual thalamus. *Nat. Commun.* **9**, 4882 (2018).

56. C. M. Niell, M. P. Stryker, Modulation of visual responses by behavioral state in mouse visual cortex. *Neuron* **65**, 472–479 (2010).

57. E. L. Savier, H. Chen, J. Cang, Effects of locomotion on visual responses in the mouse superior colliculus. *J. Neurosci.* **39**, 9360–9368 (2019).

58. S. Schröder, N. A. Steinmetz, M. Krumin, M. Pachitariu, M. Rizzi, L. Lagnado, K. D. Harris, M. Carandini, Arousal modulates retinal output. *Neuron* **107**, 487–495.e9 (2020).

59. B. N. Armbruster, X. Li, M. H. Pausch, S. Herlitze, B. L. Roth, Evolving the lock to fit the key to create a family of G protein-coupled receptors potently activated by an inert ligand. *Proc. Natl. Acad. Sci. U.S.A.* **104**, 5163–5168 (2007).

60. E. S. Boyden, F. Zhang, E. Bamberg, G. Nagel, K. Deisseroth, Millisecond-timescale, genetically targeted optical control of neural activity. *Nat. Neurosci.* **8**, 1263–1268 (2005).

61. B. L. Roth, DREADDs for neuroscientists. *Neuron* **89**, 683–694 (2016).

62. A. Mathis, P. Mamidanna, K. M. Cury, T. Abe, V. N. Murthy, M. W. Mathis, M. Bethge, DeepLabCut: Markerless pose estimation of user-defined body parts with deep learning. *Nat. Neurosci.* **21**, 1281–1289 (2018).

63. P. J. May, M. A. Basso, Connections between the zona incerta and superior colliculus in the monkey and squirrel. *Brain Struct. Funct.* **223**, 371–390 (2018).

64. M. E. Bickford, N. Zhou, T. E. Krahe, G. Govindaiah, W. Guido, Retinal and tectal "driver-like" inputs converge in the shell of the mouse dorsal lateral geniculate nucleus. *J. Neurosci.* **35**, 10523–10534 (2015).

65. G. De Franceschi, S. G. Solomon, Visual response properties of neurons in the superficial layers of the superior colliculus of awake mouse. *J. Physiol.* **596**, 6307–6332 (2018).

66. L. Wang, R. Sarnaik, K. Rangarajan, X. Liu, J. Cang, Visual receptive field properties of neurons in the superficial superior colliculus of the mouse. *J. Neurosci.* **30**, 16573–16584 (2010).

67. R. Beltramo, M. Scanziani, A collicular visual cortex: Neocortical space for an ancient midbrain visual structure. *Science* **363**, 64–69 (2019).

68. Q. Wang, A. Burkhalter, Stream-related preferences of inputs to the superior colliculus from areas of dorsal and ventral streams of mouse visual cortex. *J. Neurosci.* **33**, 1696–1705 (2013).

69. J. Graham, An autoradiographic study of the efferent connections of the superior colliculus in the cat. *J. Comp. Neurol.* **173**, 629–654 (1977).

70. Q. Wang, S.-L. Ding, Y. Li, J. Royall, D. Feng, P. Lesnar, N. Graddis, M. Naeemi, B. Facer, A. Ho, T. Dolbeare, B. Blanchard, N. Dee, W. Wakeman, K. E. Hirokawa, A. Szafer, S. M. Sunkin, S. W. Oh, A. Bernard, J. W. Phillips, M. Hawrylycz, C. Koch, H. Zeng, J. A. Harris, L. Ng, The Allen Mouse Brain Common Coordinate Framework: A 3D reference atlas. *Cell* **181**, 936–953.e20 (2020).

71. A. Sumser, M. Joesch, P. Jonas, Y. Ben-Simon, Fast, high-throughput production of improved rabies viral vectors for specific, efficient and versatile transsynaptic retrograde labeling. *eLife* **11**, e79848 (2022).

72. K. Morimoto, D. C. Hooper, S. Spitsin, H. Koprowski, B. Dietzschold, Pathogenicity of different rabies virus variants inversely correlates with apoptosis and rabies virus glycoprotein expression in infected primary neuron cultures. *J. Virol.* **73**, 510–518 (1999).

73. T. R. Reardon, A. J. Murray, G. F. Turi, C. Wirblich, K. R. Croce, M. J. Schnell, T. M. Jessell, A. Losonczy, Rabies virus CVS-N2c(ΔG) strain enhances retrograde synaptic transfer and neuronal viability. *Neuron* **89**, 711–724 (2016).

74. B. Zingg, X.-L. Chou, Z.-G. Zhang, L. Mesik, F. Liang, H. W. Tao, L. I. Zhang, AAV-mediated anterograde transsynaptic tagging: Mapping corticocollicular input-defined neural pathways for defense behaviors. *Neuron* **93**, 33–47 (2017).

75. X. Chou, X. Wang, Z. Zhang, L. Shen, B. Zingg, J. Huang, W. Zhong, L. Mesik, L. I. Zhang, H. W. Tao, Inhibitory gain modulation of defense behaviors by zona incerta. *Nat. Commun.* **9**, 1151 (2018).

76. S. Hormigo, J. Zhou, M. A. Castro-Alamancos, Zona incerta GABAergic output controls a signaled locomotor action in the midbrain tegmentum. *eNeuro* **7**, ENEURO.0390-19.2020 (2020).

77. X. Wang, X. Chou, B. Peng, L. Shen, J. J. Huang, L. I. Zhang, H. W. Tao, A cross-modality enhancement of defensive flight via parvalbumin neurons in zona incerta. *eLife* **8**, e42728 (2019).

78. Z.-D. Zhao, Z. Chen, X. Xiang, M. Hu, H. Xie, X. Jia, F. Cai, Y. Cui, Z. Chen, L. Qian, J. Liu, C. Shang, Y. Yang, X. Ni, W. Sun, J. Hu, P. Cao, H. Li, W. L. Shen, Zona incerta GABAergic neurons integrate prey-related sensory signals and induce an appetitive drive to promote hunting. *Nat. Neurosci.* **22**, 921–932 (2019).

79. A. Adhikari, T. N. Lerner, J. Finkelstein, S. Pak, J. H. Jennings, T. J. Davidson, E. Ferenczi, L. A. Gunaydin, J. J. Mirzabekov, L. Ye, S.-Y. Kim, A. Lei, K. Deisseroth, Basomedial amygdala mediates top-down control of anxiety and fear. *Nature* **527**, 179–185 (2015).

80. M. R. Milad, G. J. Quirk, Neurons in medial prefrontal cortex signal memory for fear extinction. *Nature* **420**, 70–74 (2002).

81. M. R. Milad, G. J. Quirk, Fear extinction as a model for translational neuroscience: Ten years of progress. *Annu. Rev. Psychol.* **63**, 129–151 (2012).

82. J. Jhang, H. Lee, M. S. Kang, H.-S. Lee, H. Park, J.-H. Han, Anterior cingulate cortex and its input to the basolateral amygdala control innate fear response. *Nat. Commun.* **9**, 2744 (2018).

83. N. H. Kalin, S. E. Shelton, A. S. Fox, T. R. Oakes, R. J. Davidson, Brain regions associated with the expression and contextual regulation of anxiety in primates. *Biol. Psychiatry* **58**, 796–804 (2005).

84. D. Mobbs, M. A. Eckert, D. Mills, J. Korenberg, U. Bellugi, A. M. Galaburda, A. L. Reiss, Frontostriatal dysfunction during response inhibition in Williams syndrome. *Biol. Psychiatry* **62**, 256–261 (2007).

85. A. J. Shackman, T. V. Salomons, H. A. Slagter, A. S. Fox, J. J. Winter, R. J. Davidson, The integration of negative affect, pain and cognitive control in the cingulate cortex. *Nat. Rev. Neurosci.* **12**, 154–167 (2011).

86. U. Kim, E. Gregory, W. C. Hall, Pathway from the zona incerta to the superior colliculus in the rat. *J. Comp. Neurol.* **321**, 555–575 (1992).

87. A. Dubreuil, A. Valente, M. Beiran, F. Mastrogiuseppe, S. Ostojic, The role of population structure in computations through neural dynamics. *Nat. Neurosci.* **25**, 783–794 (2022).

88. D. de Malmazet, N. K. Kühn, K. Farrow, Retinotopic separation of nasal and temporal motion selectivity in the mouse superior colliculus. *Curr. Biol.* **28**, 2961–2969.e4 (2018).

89. T. Baden, P. Berens, K. Franke, M. Román Rosón, M. Bethge, T. Euler, The functional diversity of retinal ganglion cells in the mouse. *Nature* **529**, 345–350 (2016).

90. N. Fachada, V. Lopes, R. Martins, A. Rosa, micompr: An R package for multivariate independent comparison of observations. *R J.* **8**, 405–420 (2016).

91. M. Pachitariu, C. Stringer, M. Dipoppa, S. Schröder, L. F. Rossi, H. Dalgleish, M. Carandini, K. D. Harris, Suite2p: Beyond 10,000 neurons with standard two-photon microscopy. bioRxiv 061507 [Preprint] 20 July 2017. https://doi.org/10.1101/061507.

Science Advances

Pathway-specific inputs to the superior colliculus support flexible responses to visual threat

Chen Li, Norma K. Kühn, Ilayda Alkislar, Arnau Sans-Dublanc, Firdaouss Zemmouri, Soraya Paesmans, Alex Calzoni, Frédérique Ooms, Katja Reinhard, and Karl Farrow

View the article online
https://www.science.org/doi/10.1126/sciadv.ade3874
Permissions
https://www.science.org/help/reprints-and-permissions

Use of this article is subject to the Terms of service